Nano Research

ISSN 1998-0124 CN 11-5974/O4
https://doi.org/10.26599/NR.2025.94907347

Research Article

Bandgap engineering of halide perovskite nanoribbons for high-performance photodetection

Pengfei Guo[1,2](✉), Jishen Wang[1], Xia Shen[1], Qihang Lv[1], Xuyang Li[1], Zitong Xu[1], Shuangping Han[1], Yaoxing Bian[1], You Meng[4], Lingzhen Yang[1], Chengbing Qin[3], Kin Man Yu[6,7], Johnny C Ho[2,5], Liantuan Xiao[1](✉)

[1] College of Physics and Optoelectronics, Taiyuan University of Technology, Taiyuan 030024, China

[2] Department of Materials Science and Engineering, City University of Hong Kong, Kowloon, Hong Kong 999077, China

[3] State Key Laboratory of Quantum Optics and Quantum Optics Devices, Institute of Laser Spectroscopy, Shanxi University, Taiyuan 030024, China

[4] Changsha Semiconductor Technology and Application Innovation Research Institute, College of Semiconductors (College of Integrated Circuits), Hunan University, Changsha 410082 China

[5] Institute for Materials Chemistry and Engineering, Kyushu University, Fukuoka 8819-0395, Japan

[6] Department of Physics, "National Sun Yat Sen University", Kaohsiung, Taiwan 80424, China

[7] Materials Sciences Division, Lawrence Berkeley National Laboratory, CA 94720, USA

Nano Res., **Just Accepted Manuscript** • https://doi.org/10.26599/NR.2025.94907347
https://www.sciopen.com/journal/1998-0124 on Mar. 5, 2025

Research Article **https://doi.org/10.26599/NR.2025.94907347**

Bandgap engineering of halide perovskite nanoribbons for high-performance photodetection

Pengfei Guo[1,2,*], Jishen Wang[1], Xia Shen[1], Qihang Lv[1], Xuyang Li[1], Zitong Xu[1], Shuangping Han[1], Yaoxing Bian[1], You Meng[4], Lingzhen Yang[1], Chengbing Qin[3], Kin Man Yu[6,7], Johnny C. Ho[2,5], and Liantuan Xiao[1,*]

[1]College of Physics and Optoelectronics, Taiyuan University of Technology, Taiyuan 030024, China

[2]Department of Materials Science and Engineering, City University of Hong Kong, Kowloon, Hong Kong 999077, China

[3]State Key Laboratory of Quantum Optics and Quantum Optics Devices, Institute of Laser Spectroscopy, Shanxi University, Taiyuan 030024, China

[4]Changsha Semiconductor Technology and Application Innovation Research Institute, College of Semiconductors (College of Integrated Circuits), Hunan University, Changsha 410082 China

[5]Institute for Materials Chemistry and Engineering, Kyushu University, Fukuoka 8819-0395, Japan

[6]Department of Physics, "National Sun Yat Sen University", Kaohsiung, Taiwan 80424, China

[7]Materials Sciences Division, Lawrence Berkeley National Laboratory, CA 94720, USA

Received: 6 February 2025; Revised: 27 February 2025; Accepted: 4 March 2025

✉**Address correspondence to** Pengfei Guo**,** guopengfei2010@126.com; Liantuan Xiao**,** xlt@sxu.edu.cn

Cite this article: *Nano Research*, 2025, 18, 94907347.

https://doi.org/10.26599/NR.2025.94907347

Abstract: Bandgap engineering of semiconductor nanowires or nanoribbons (NRs) offers a promising material foundation for multifunctional integrated optoelectronic devices and circuits. Among these materials, all-inorganic halide perovskites have emerged as a leading candidate for next-generation photoelectronic applications due to their outstanding optoelectronic properties. In this work, we report the direct synthesis of high-quality bandgap gradient lead halide perovskite ($CsPbCl_{3(1-x)}Br_{3x}$ and $CsPbBr_{3(1-x)}I_{3x}$ (X = 0-1) NRs using a magnetic-pulling source-moving chemical-vapor-deposition (CVD) method. Microstructural characterizations reveal that these as-grown NRs possess high-quality single crystalline structures with continuously tunable compositions. The photoluminescence emissions of these perovskite NRs can be finely tuned across the entire visible spectrum (417-702 nm). Furthermore, photodetectors based on these perovskite NRs demonstrate exceptional photoelectric performance, including a high I_{ON}/I_{OFF} ratio (10^4), superior responsivity (37.5 A/W), and remarkable detectivity (2.81×10^{13} Jones). A spatially resolved imaging sensor based on these perovskite NRs is also demonstrated, indicating promising applications in photoelectronic imaging circuits. These bandgap-tunable perovskite NRs provide a versatile materials platform for future integrated devices in electronics and optoelectronics.

Keywords: perovskite nanoribbons, anion exchange process, one-step chemical-vapor-deposition, bandgap engineering, photodetector

1 Introduction

Halide perovskites have attracted significant attention due to their exceptional optoelectronic properties, such as extended carrier lifetimes, high photoluminescence (PL) quantum yields, and efficient charge transfer. [1-3] These characteristics make halide perovskites ideal material platforms for integrated circuits, including solar cells, [4-6] light-emitting diodes (LEDs), [7-9] lasers, [10-13] photodetectors, [14-18] optical waveguides [19-20]and more. Traditional semiconductors with single and limited bandgap structures face numerous limitations in the application of integrated optoelectronic devices and circuits. In contrast, the bandgaps of alloy semiconductors can be engineered and tailored to meet diverse application requirements. [21-22] In this context, the anion exchange method has proven to be a simple and versatile approach for achieving precise control over material compositions. [23-27] Specifically, perovskites possess a soft dynamic lattice and low defect formation energy due to their fragile ionic bonds and high vacancy concentrations, which allow ions to diffuse and migrate within the lattice. This makes them ideal materials for bandgap-engineered alloy structures. [28-30]

Adjusting the compositions of halide perovskites through ion exchange processes is an effective way to regulate the bandgaps of these semiconductors. For instance, in 2017, Yang et al. reported a three-component heterojunction based on a single nanowire $CsPbX_3$ (X = Cl, Br, I), achieved through partial structure masking and anion exchange. [27] In 2020, Tang et al. constructed a single perovskite alloy nanowire using solid-state anion diffusion technology, which was utilized for a range of continuous wavelength-tunable lasers. [31] In 2022, Li et al. reported a spatially resolved one-dimensional single Y-$CsPbI_3$ nanowire through an anion exchange process, which exhibited the formation of a sharp heterojunction at lower temperatures. [32] Moreover, $CsPbCl_{3-x}Br_x$ microdisk laser arrays and $CsPb_xSn_{1-x}(Br_yI_{1-y})_3$ nanowires have also been successfully realized using the anion exchange method. [33, 34] Despite the significant

advantages of perovskite structures in optoelectronics, synthesizing and applying bandgap-continuous gradient perovskite nanoribbons (NRs) with emissions covering the entire visible range remains challenging.

Compared to three-dimensional perovskite bulks and polycrystalline films, perovskite nanoribbons offer a more direct charge transfer path, which benefits charge carrier collection. The larger effective area of NRs enhances photodetectors' performance, providing higher switch ratios, responsivity, and detectivity. [35-38] In this work, we report the successful synthesis of bandgap-continuous tunable all-inorganic halide perovskite NRs using a developed magnetic-pulling source replaced chemical-vapor-deposition approach. Structural characterization of these as-grown NRs reveals a regular stripe structure with tunable compositions and high-quality crystallinity. Spatially resolved photoluminescent spectra and PL mapping of these ribbons show wavelength-continuous tunable emissions from 417 to 702 nm, nearly covering the entire visible range. High-performance photodetectors based on these perovskite NRs were constructed and systematically investigated, demonstrating high responsivity (37.5 A W^{-1}), high detectivity (2.81×10^{13} Jones), fast response times (16 ~ 17 ms), and high external quantum efficiency (EQE) (7×10^{3} %). Moreover, a spatially resolved image sensor based on compositional gradient perovskite NRs was demonstrated to have excellent imaging capability, indicating promising application prospects in future optoelectronic imaging circuits. These results suggest that bandgap-graded perovskite NRs provide an attractive material platform for integrated photonics and optoelectronic devices.

2 Experimental

2.1 Synthesis of pure $CsPbCl_3$, $CsPbBr_3$, and $CsPbI_3$ NRs:

A magnetic-pulling source-moving CVD system was used to synthesize inorganic halide perovskite NRs, as schematically shown in Figure. S1 (See Electronic Supplementary Material and Experimental). Powder sources and reagents were purchased from Alfa Aesar. A horizontal furnace (OTF-1200X) with a quartz tube (inner diameter 45 mm, length 180 cm) was used during the experiment. Before growth, $CsBr/PbBr_2$ powder sources (molar ratio=2:1) were mixed and placed in a quartz boat in the center and upstream of the heating zone A. The product was collected on the Si/SiO_2 substrates (4 mm × 10 mm) at the deposition area in the center of healing zone B. 0.1 mg ml^{-1} Sn solution was dropped onto the substrates as a catalyst before the growth. Before heating, N_2 gas was introduced into the system at a flow rate of 60 sccm for 30 min to purge the air and moisture from the tube. Then, the carrier gas (40 sccm H_2 and 40 sccm N_2) was introduced into the system, and the pressure was maintained at 5.8 torr. The $CsPbX_3$ source powder was placed inside the heating zone A with temperature settings of 420 ℃ ($CsPbI_3$), 430 ℃ ($CsPbBr_3$), and 460 ℃ ($CsPbCl_3$). The substrates were placed inside heating zone B with temperature settings of 290 ℃ ($CsPbI_3$), 330 ℃ ($CsPbBr_3$), and 350 ℃ ($CsPbCl_3$) at a rate of 25 ℃ min^{-1}, respectively. After the growth, the temperature was naturally reduced to room temperature.

2.2 Synthesis of alloyed perovskite NRs:

A first quartz boat with the mixture of $PbBr_2/CsBr$ powder (mole ratio= 1:2, Alfa Aesar, 99.9 %) at the centre of heating area. A second quartz boat with the mixture of PbX_2/CsX powder (X = Cl or I, mole ratio =1:2, Alfa Aesar, 99.9 %) was placed away from the heating zone of the furnace before growth. Both quartz boats with powder sources were connected by a quartz rod with sufficient distance between them (Figure S1, See the Supporting Information). Moreover, the stepper motor (Zolix, PA 100) and the reaction source replacement device are connected by

magnets. The stepper motor with the magnet runs 30 cm at a constant speed of 20 cm min^{-1} to achieve the replacement of the reaction source. After 60 min growth of the first step, the furnace temperature was reduced to 440 °C ($CsPbCl_{3(1-x)}Br_{3x}$) or 420 °C ($CsPbBr_{3(1-x)}I_{3x}$). The second boat was pushed into the left zone to replace the former boats at a rate of 20 cm min^{-1} by a stepping motor. The carrier gas (40 sccm H_2 and 40 sccm N_2) was introduced into the system, and the growth pressure of the nanoribbons was controlled around 5.8 Torr at the entire experimental process. Under high temperatures, these perovskite alloy NRs are composed by controlling the growth time during the second growth process. The relationship between anion exchange time and components is shown in Figure. S1**.**

2.3 Characterization:

The scanning electron microscope (SEM, Hitachi, SU-8010, Japanese) and transmission electron microscope (TEM, JEM-F200) were used to investigate the morphology and compositions of the perovskite NRs. Crystal structures were analyzed using the X-ray diffraction (XRD, Bruker D8) system. The optical characterizations were tested by a confocal optical system. The laser beam (375 nm, the power density of laser: 1.4×10^6 mW cm^{-2}, spot size: 1.8×10^{-8} cm^2) was focused by a microscope lens (Nikon, ×100) and locally excited at the samples. The PL spectra were recorded by an optical spectrometer (Maya Pro2000), and real-color images were recorded by a CCD camera, as shown in Figure. S2. Before the optical testing, some selected NRs were transferred to the pre-cleaned Si/SiO_2 substrates. The electrodes are completed through a metal evaporation process. The Keithley 2450 was used to investigate the constructed photodetector's current-voltage (I-V) characteristics. The imaging sensors were investigated under a two-dimensional electric displacement table (Zolix-SC300). A signal generator (DG822, Rigol) was used during the optical communication test, providing the output signal to the laser.

3 Results and discussion

Some typical $CsPbBr_3$ NRs were selected for structural characterizations, as shown in Figure. 1. Figure. 1a and the inset images show the low- and high-resolution scanning electron microscopy (SEM) images of the $CsPbBr_3$ NRs, respectively. More selected SEM images and elemental profiles of $CsPbX_3$ ribbons are shown in Figure. S3 and S4 (Supporting information). The length and the width of the perovskite NRs are ~5-20 μm and ~2-5 μm, respectively, according to the structural investigation. High-resolution SEM images and the energy-dispersive X-ray spectroscopy (EDX) mapping images of a typical pure $CsPbBr_3$ NR are shown in Figure. 1b. As can be seen, Cs, Pb, and Br exhibit a uniform distribution along the length of the ribbon. Figure. 1c shows the EDX spectra at two typical positions (Spot 1 and Spot 2) along a single ribbon, which shows the elements (Cs, Pb, and Br) ratio about 1:1:3, showing well agreement with pure $CsPbX_3$ perovskite structures. Figure. 1d shows the EDX line scanning profiles of the same NR along the axial direction, which shows agreement with the two-dimensional (2-D) EDX elemental mapping in Figure. 1b. Notably, Pb exhibits a sudden increase at the tip of the NR, which indicates that the catalyst nanosphere at the tip of the NR is mainly composed of Pb. Meanwhile, the catalysts can also be observed at the tips of some NRs, as shown in Figure. S4 (Supporting information). This is consistent with the previously reported phenomenon of a catalyst-assisted vapor-liquid-solid (V-L-S) growth mechanism. [18, 19] Figure. 1e shows the XRD patterns of the composition gradient perovskite alloyed NRs, ranging from 10 to 50°. The sharp diffraction peaks in Figure. 1e and Figure. 1f confirms that these composition-tunable $CsPbX_3$ alloyed nanostructures have high-quality crystalline. The XRD results indicate that $CsPbCl_3$, $CsPbBr_3$, and $CsPbI_3$ NRs are indexed to tetragonal, cubic, and orthorhombic phases, respectively, which shows good agreement with the previously reported structures. [39, 40] The strong (100) diffraction peaks of $CsPbCl_3$ and $CsPbBr_3$ samples shift significantly towards lower diffraction angles with the increase of Br and I in the corresponding $CsPbCl_{3(1-x)}Br_{3x}$ and

$CsPbBr_{3(1-x)}I_{3x}$ alloys structures, respectively, which indicates that halogen ions completely diffuse with each other during the growth process, forming a random alloy without phase separation. [39] The XRD results of these alloyed $CsPbX_3$ NRs with different compositions show good agreement with the EDX profiles of the perovskite NRs, as shown in Figure. S5. (Supporting information). For example, Figure. 1g shows the low-resolution TEM image of a typical $CsPbBr_3$ NR, which shows a length and width of about 22 μm and 3 μm, respectively. Figure. 1h and 1i show the high-resolution TEM (HR-TEM) images at two typical positions (the red box and blue box in Figure. 1e) along the length of a typical ribbon. Inter planar spacing of the $CsPbBr_3$ NR is measured for 0.290 nm, consistent with the (200) plane of the cubic phase $CsPbBr_3$. [41-43] The fast Fourier transform (FFT) method obtained the inset, indicating that the $CsPbBr_3$ NRs are in a well-organized cubic phase, which is in good agreement with the XRD measurements. These results show that the as-grown $CsPbCl_{3(1-x)}Br_{3x}$ and $CsPbBr_{3(1-x)}I_{3x}$ alloy structures are composition-graded NRs with high-quality crystalline.

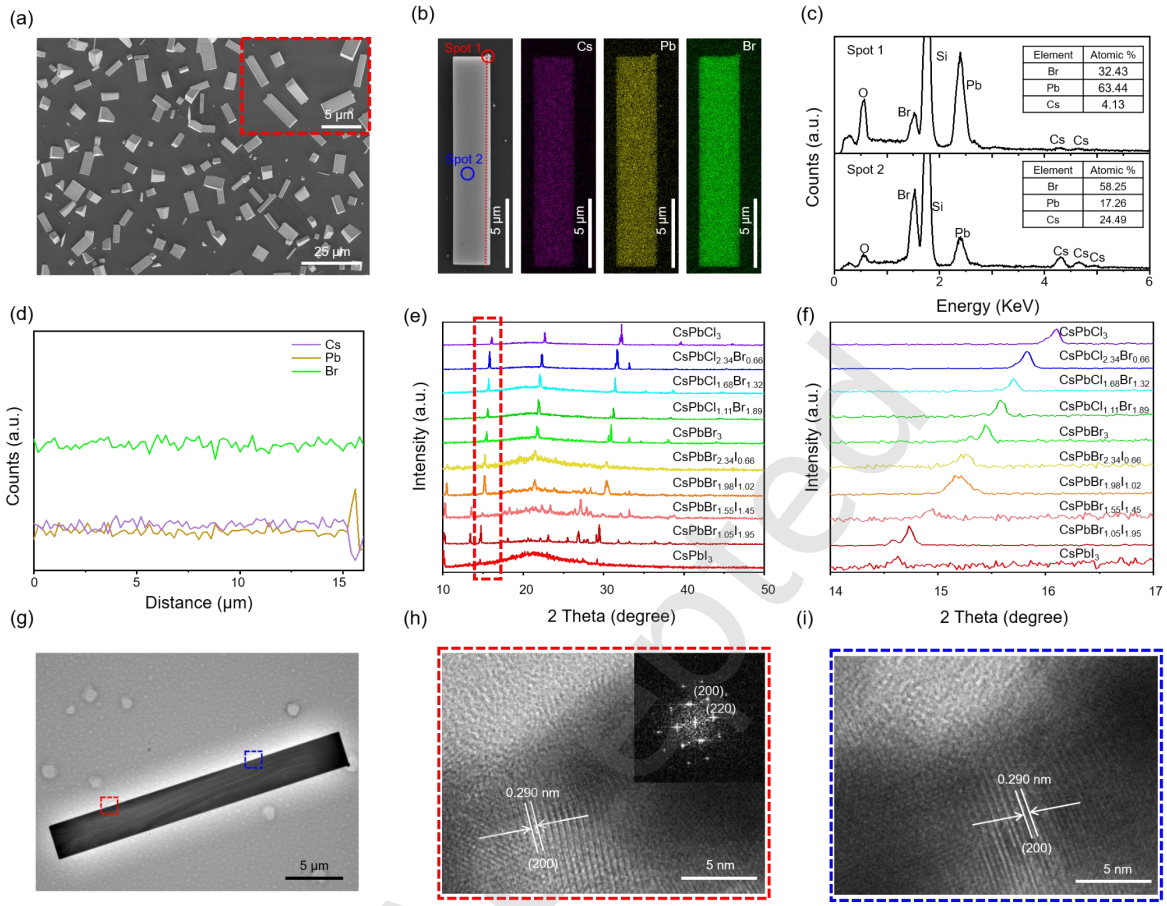

Figure 1. Structural characterizations of a typical $CsPbBr_3$ NR. (a) Low- and high-resolution (inset) top-view SEM images of $CsPbBr_3$ perovskite NRs grown on the Si/SiO_2 substrate. (b) SEM image and EDX element mapping of a typical $CsPbBr_3$ NR. (c) EDX spectra at two typical positions (spot 1 and spot 2) of a $CsPbBr_3$ NR, as indicated in (b). (d) EDX line scans EDX profiles along the axial direction of an NR (dotted line as shown in (b)). (e) XRD patterns of the bandgap gradient $CsPbCl_{3(1-x)}Br_{3x}$ and $CsPbBr_{3(1-x)}I_{3x}$ (X = 0-1) NRs ranging from 10 to 50°. (f) Enlarged XRD pattern ranging from 14 to 17°. (g) Low-resolution TEM image of a typical $CsPbBr_3$ NR. (h, i) High-resolution TEM images of two typical positions along the ribbon (inset shows the corresponding FFT patterns of $CsPbBr_3$ NRs).

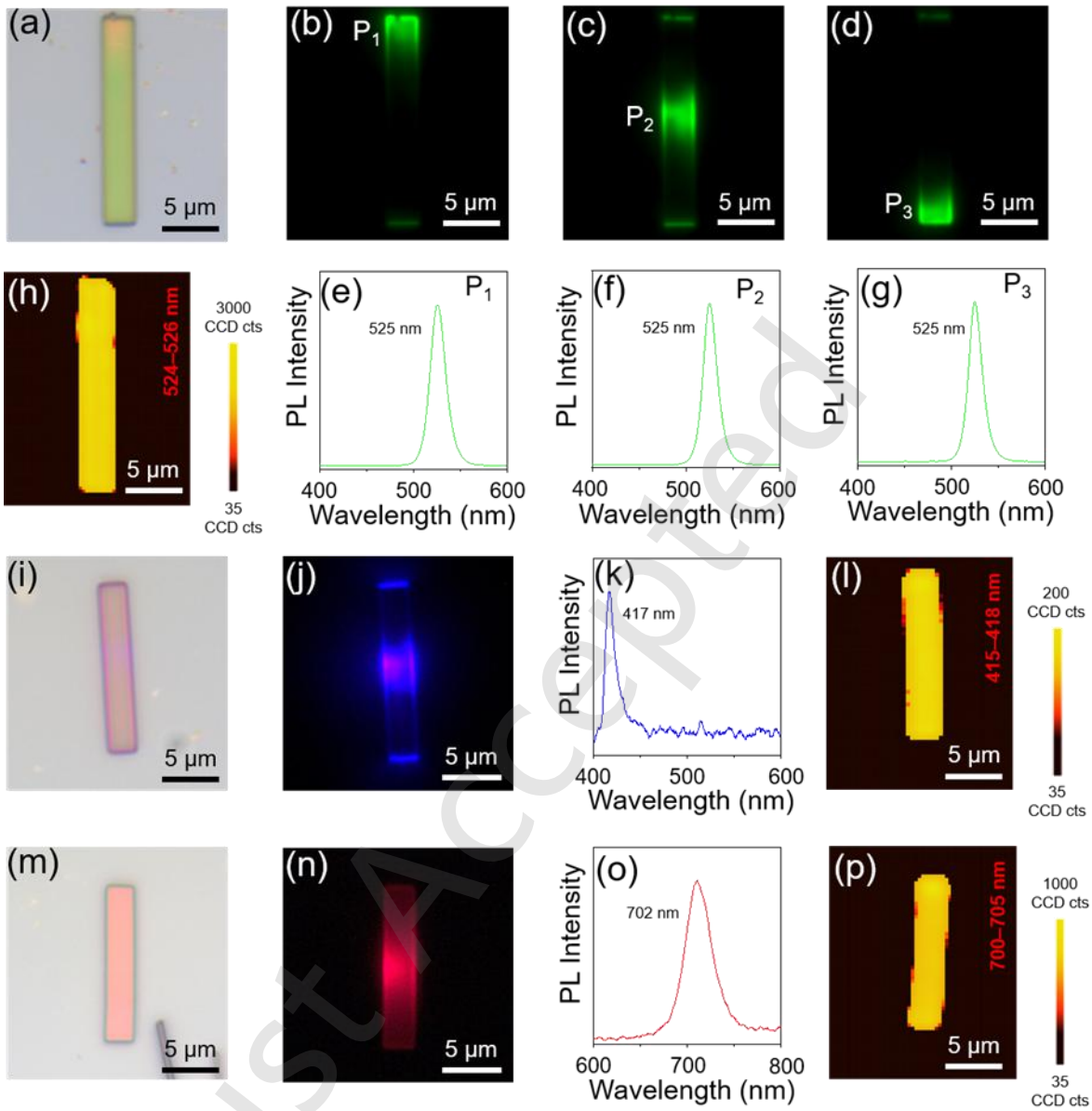

Figure 2. Optical characterizations of the bandgap tunable $CsPbX_3$ (X = Cl, Br, and I) NRs. (a) Optical image of a typical $CsPbBr_3$ NR. (b-d) Dark-field real-color images of the $CsPbBr_3$ NR excited by a focused 375 nm laser at three typical positions (P_1-P_3), respectively. (h) 2D PL mapping of a selected $CsPbBr_3$ NR in (a) (scanning wavelength ranges are 524-526 nm). (e-g) The corresponding PL spectra at three typical positions (P_1-P_3), respectively. (i, m) Optical photographs, (j, n) dark-field images, and (l, p) corresponding PL spectra of the $CsPbCl_3$ and

$CsPbI_3$ NRs, respectively. (k, o) 2D PL mapping of the $CsPbCl_3$ (scanning wavelength ranges are 415-418 nm) and $CsPbI_3$ (scanning wavelength ranges are 700-705 nm) NRs, respectively.

The room-temperature optical properties of these NRs were studied by a confocal optical microscopy system, as shown in Figure. S2 (Supporting information). PL spectral characterizations, including dark-field real-color images and PL mapping of the typical perovskite NRs, are shown in Figure. 2. Figure. 2a-2d shows the top-view optical photograph and dark-field real-color images of a typical $CsPbBr_3$ NR, respectively. A 375 nm continuous wavelength (CW) laser is used and focused on the samples as the exciting light. 2-D PL mapping (Figure. 2e) of the $CsPbBr_3$ NR shows a uniform emission along the ribbon, which exhibits a perfect belt-like structure. Figure. 2f-2h shows the corresponding PL emission spectra of three typical positions (P_1–P_3) from the $CsPbBr_3$ NR, which have emission peaks centered at 525 nm, showing well agreement with the real-color images in Figure. 2b-2d, respectively. Figure. 2i and 2m show the optical images and dark-field real-color images of the pure $CsPbCl_3$ and $CsPbI_3$ NRs, respectively. Dark-field images of the $CsPbCl_3$ and $CsPbI_3$ NRs are shown in Figure. 2j and 2n; bright blue and red emissions can be observed from the two ribbons under a 375 nm laser irradiation. Meanwhile, an optical waveguide can be observed at both ends of the NRs. Figure. 2k, o, l, and p show the 2-D PL mapping and PL spectra of $CsPbCl_3$ and $CsPbI_3$ NRs, indicating PL emission centered at 417 and 702 nm, respectively. The PL spectra detected from a single NR show that the full width at half maximum (FWHM) of $CsPbCl_3$, $CsPbBr_3$, and $CsPbI_3$ nanowires are about 10 nm, 16 nm, and 31 nm, respectively, suggesting that these pure $CsPbX_3$ NRs may have good crystalline quality without obvious defects. [42-45].

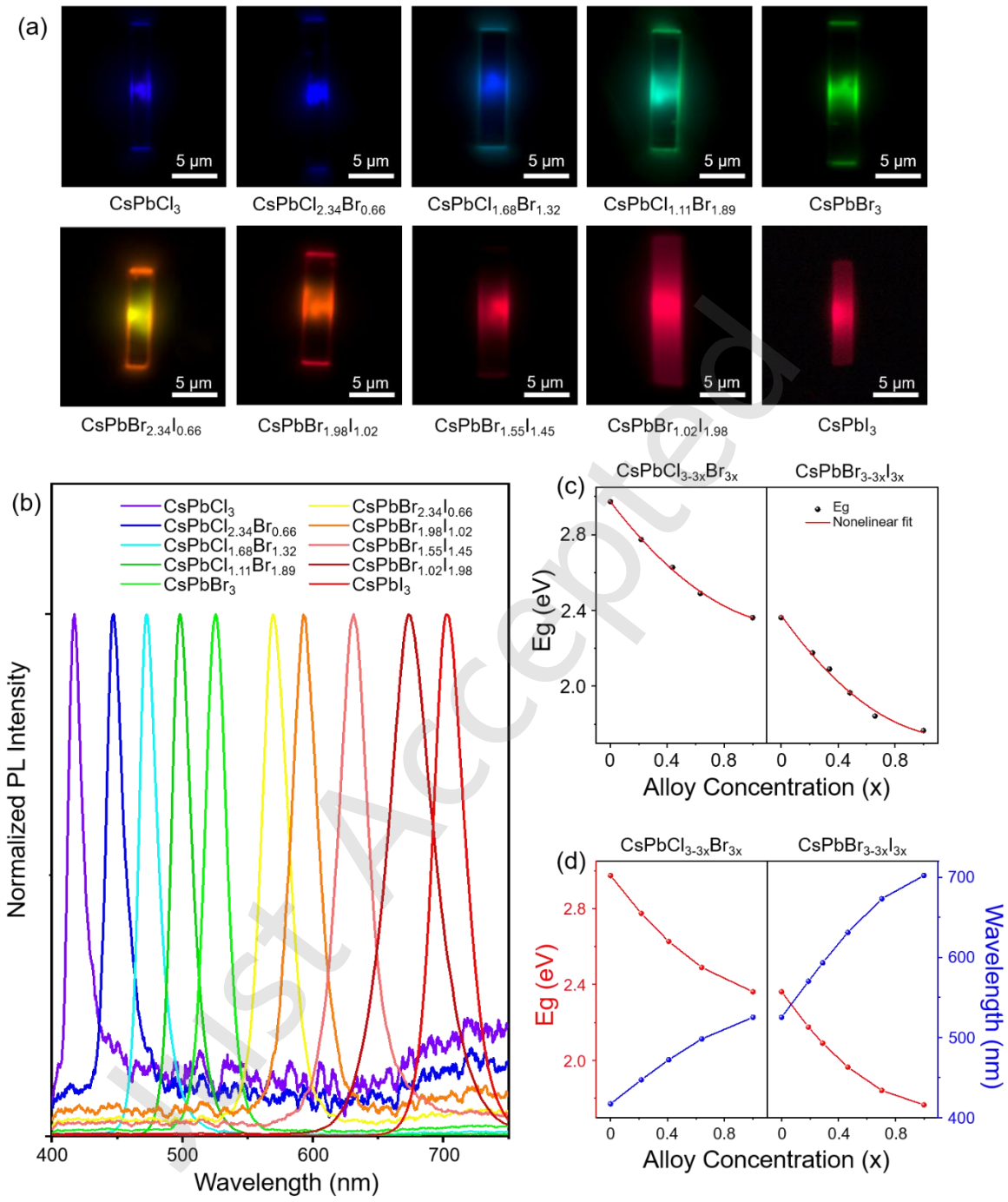

Figure 3. Optical properties of bandgap gradient perovskite $CsPbX_3$ alloy NRs. (a) Dark-field real-color images and (b) corresponding PL spectra of bandgap gradient $CsPbCl_{3(1-x)}Br_{3x}$ and $CsPbBr_{3(1-x)}I_{3x}$ (X = 0-1) alloy NRs with different components excited by a 375 nm laser beam. The scale bar is 5 μm. (c) The relationship between bandgaps and compositions of Br ratio in

alloy NRs obtained by the EDX profiles. The black square represents the experimental data Eg, and the solid red line represents the fitting line. (d) The relationship between emission wavelength and bandgap of the $CsPbCl_{3(1-x)}Br_{3x}$ and $CsPbBr_{3(1-x)}I_{3x}$ (X = 0-1) alloy NRs. The red and blue circles represent the bandgaps of $CsPbX_3$ NRs and the wavelength of the emission peaks, respectively.

The composition-dependent optical properties of these perovskite alloyed NRs are investigated, as shown in Figure. 3. Figure. 3a exhibits the dark-field real-color images of the $CsPbCl_{3(1-x)}Br_{3x}$ and $CsPbBr_{3(1-x)}I_{3x}$ (X = 0-1) alloyed NRs under a 375 nm laser excitation, which exhibits a color tunable emissions from blue to green and red, respectively. The corresponding PL spectra in Figure. 3b shows that the emission peaks of these alloyed NRs are continuously changed from 417 nm to 702 nm, nearly covering the entire visible range. The bright luminescence at both ends of the NRs is obviously observed under focused laser excitation, suggesting good waveguide properties of the perovskite NRs. Notably, the FWHM of the PL emission peaks in Figure. 3b is about 10~35nm, suggesting that these as-grown NRs synthesized using a CVD strategy may have high crystallization. [46] Figure. 3c shows the relationship between the component x and the bandgap values of the $CsPbCl_{3x}Br_{3-3x}$ and $CsPbBr_{3x}I_{3-3x}$ alloyed ribbons obtained through the EDX profiles (Figure. S3, Electronic Supplementary Material and Experimental). The relationship is shown as follows:

$$Eg(A_xB_{1-x}) = xEg(A) + (1-x)Eg(B) - bx(1-x) \quad (1)$$

For Cl/Br and Br/I alloys, the compositional dependence of the bandgap can be expressed as:

$$Eg(CsPbCl_{3-3x}Br_{3x}) = xE_g(CsPbBr_3) + (1-x)E_g(CsPbCl_3) - bx(1-x) \quad (2)$$

$$Eg(CsPbBr_{3-3x}I_{3x}) = xEg(CsPbI_3) + (1-x)Eg(CsPbBr_3) - bx(1-x) \quad (3)$$

where x represents the proportion of Br element components, and b represents the bending parameter of the curve. *Eg* = 2.974, 2.362, and 1.767 eV represent the bandgaps of $CsPbCl_3$, $CsPbBr_3$, and $CsPbI_3$, respectively. Finally, the relationship curve between the bandgap of $CsPbX_3$ and Br element content is obtained. According to the calculation results, the values of $b_{Cl/Br}$ and $b_{Br/I}$ are 0.37 and 0.42, respectively, nearly equal to the previously reported results. [21, 47] Figure. 3d shows the relationship between the component Br, emission wavelength, and bandgaps of different alloy NRs. The solid lines represent the best fit of component-related bandgaps using nonlinear fitting. As can be seen, the EDX results are consistent with the calculated bandgap values, confirming the accurate regulation of perovskite components. These results indicate that these bandgap gradient perovskite alloy NRs show excellent luminescent performance with no obvious defect emissions, which agrees well with the structural characterizations in Figure. 2.

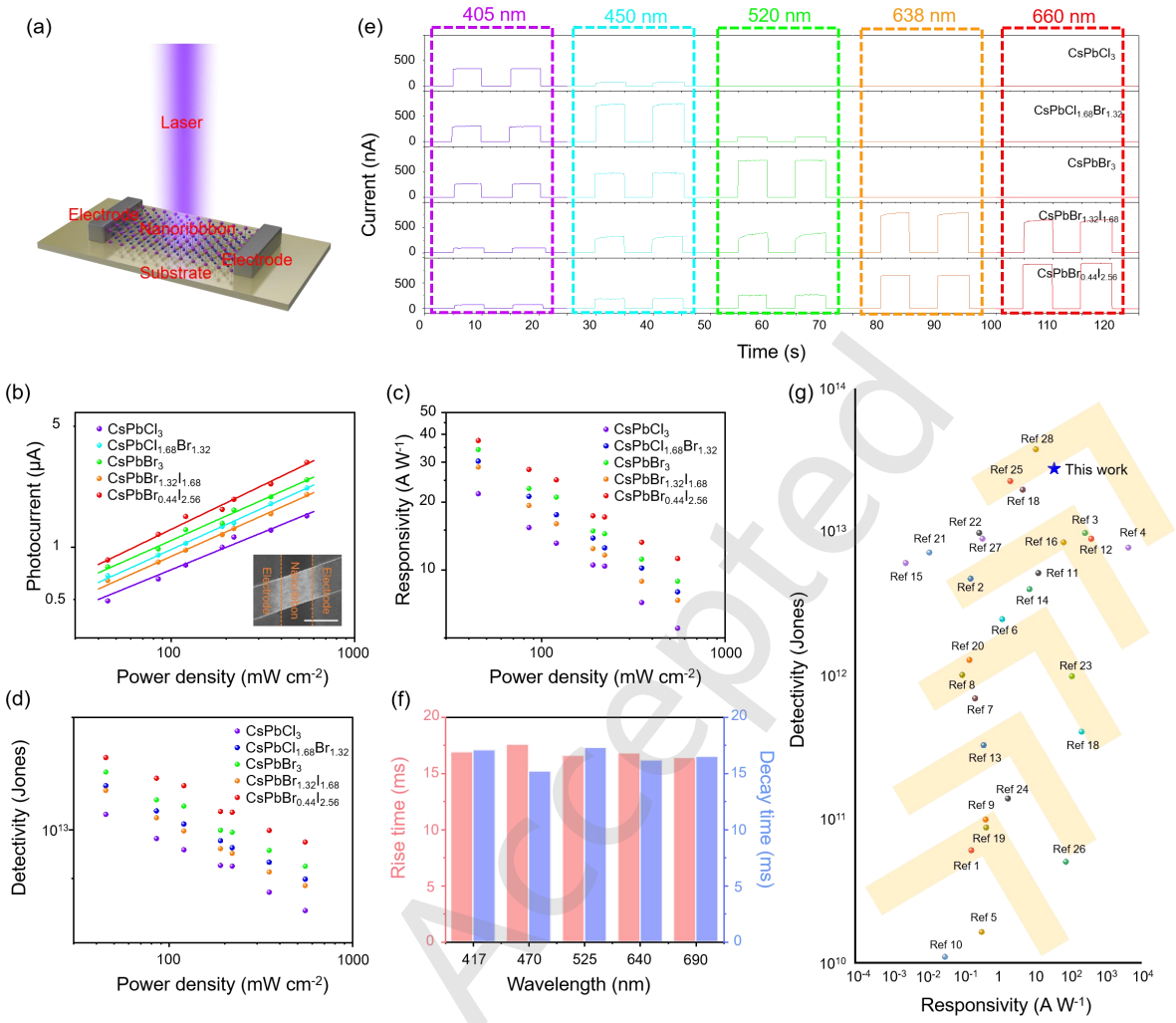

Figure 4. Photoelectrical properties of bandgap gradient $CsPbCl_{3(1-x)}Br_{3x}$ and $CsPbBr_{3(1-x)}I_{3x}$ (X = 0-1) NRs based photodetectors. (a) Schematic diagram of a photodetector based on a $CsPbX_3$ NR. (b-d) Light intensity-dependent photocurrent, responsivity, and detectivity of the different composition NR-based photodetectors. Inset shows the SEM image of the as-fabricated NRs PD, the scale bar is 6 μm. (e) The I-T curves of $CsPbCl_{3(1-x)}Br_{3x}$ and $CsPbBr_{3(1-x)}I_{3x}$ (X = 0-1) NRs-based photodetectors under various light illumination (405 nm, 450 nm, 520 nm, 638 nm and 660 nm, power density = 45 mW cm^{-2}). (f) Rise and decay time of $CsPbCl_{3(1-x)}Br_{3x}$ and $CsPbBr_{3(1-x)}I_{3x}$ (X = 0-1) NRs-based photodetectors under 405 nm, 450 nm, 520 nm, 638 nm, and 660 nm

illumination. (g) Comparison of the perovskite NR-based photodetectors' responsivity and detectivity with reported literature. Detailed performance parameters of these devices are shown in Table S1 in the Electronic Supplementary Material and Experimental.

The above discussions clearly demonstrate the successful realization of the bandgap gradient $CsPbX_3$ alloyed NRs. To demonstrate their potential optoelectronic applications, photodetectors based on these perovskite NRs were constructed on a SiO_2 substrate, and their photoconductive properties were systematically investigated. Figure. 4a shows a schematic diagram of a photodetector using an individual perovskite NR. I-V, I-T characteristics and stability testing of all devices are shown in Figure. S6-S10 (Supporting Information). Each device's I_{ON}/I_{OFF} ratio can be calculated based on the measured light and dark current values. After calculation, the I_{ON}/I_{OFF} ratios of all devices reached 10^4 or above, indicating a high performance of the devices. The SEM image of the device is shown in the inset of Figure. 4b, in which the electrodes with a gap of 5 μm are thermally deposited on both ends of the ribbon, and the thickness of the electrode is controlled at 200 nm. Detailed experimental results are shown in the Experiment Sections.

It is also noted that the laser beam with a wavelength of 660, 638, 520, 450, and 405 nm was used as the light sources for the photodetection measurement of $CsPbBr_{0.44}I_{2.56}$, $CsPbBr_{1.32}I_{1.68}$, $CsPbBr_3$, $CsPbCl_{1.68}Br_{1.32}$, and $CsPbCl_3$ NR photodetectors, respectively. The responsivity (R) and detectivity (D^*) are two critical parameters to assess the performance of photodetectors, which can be calculated by the equations as follows: [48, 49]

$$R = \frac{I_{ph}}{PA} \tag{4}$$

$$D^* = R\sqrt{\frac{A}{2eI_{dark}}} \tag{5}$$

where I_{ph} is the difference between the photocurrent and dark current, P = 45 mW cm^{-2} is the incident light power density illuminated at the periodic superstructures, A is an effective irradiated area on the device, and e is the electronic charge. Both R and D^* increase dramatically with a decrease in the light intensity. After measurement, the A values of all devices are concentrated around 4×10^{-7} cm^2. Figure. 4b to 4d depict the values of I_{ph}, R, and D^* at different light intensities. It shows that both R and D^* increase dramatically with the decreasing light intensity. Notably, photocurrent and light intensity of the NRs-based photodetectors are observed as a sublinear relationship, which may originate from the complex processes of electron − hole generation, trapping, and recombination in the nanostructures. [17, 50] Under a lower light intensity of 45 mW cm^{-2}, the R values of the perovskite alloyed NRs-based photodetectors can reach 37.5, 28.6, 34.4, 30.4, and 21.8 A W^{-1}, respectively. At the same time, the corresponding D^* values are up to 2.81×10^{13}, 1.76×10^{13}, 2.29×10^{13}, 1.88×10^{13}, and 1.25×10^{13} Jones, the I_{dark} of different nanoribbons at 2 V bias is 1.33 pA ($CsPbBr_{0.44}I_{2.56}$), 1.49 pA ($CsPbBr_{1.32}I_{1.68}$), 1.33 pA ($CsPbBr_3$), 1.61 pA ($CsPbCl_{1.68}Br_{1.32}$) and 1.74 pA ($CsPbCl_3$), respectively. By fitting the relationship between I_{ph} and P ($I_{ph} \propto P^k$, k represents the correlation coefficient), k is evaluated as 0.5, comparable with the previously reported photodetectors. [51] Figure. 4e shows the comparison investigation of the τ_r and τ_d of five typical perovskite alloy devices with various bandgaps. According to the results, the rise and decay times of all devices are concentrated at about 16~17 ms, which exhibits a fast response speed of the millisecond magnitude. Figure. 4f shows the photoresponse properties of five proposed perovskite devices under various light illuminations at V = 2V. All devices show significant photoelectrical response to light near their absorption edge. The photocurrent of $CsPbCl_3$, $CsPbCl_{1.68}Br_{1.32}$, and $CsPbBr_3$ NR devices are relatively lower than that of the $CsPbBr_{0.44}I_{2.56}$ and $CsPbBr_{1.32}I_{1.68}$ NR devices under the 638 and

660 nm laser illumination, which may because the energy of the external laser is much smaller than the bandgap of the three previous alloy materials. Additionally, the performances of photodetectors based on most perovskite structures reported to date are shown in Figure. 4g and Table S1 (see the Electronic Supplementary Material and Experimental), indicating that our device performance has significant advantages compared with the reported results. The external quantum efficiency (EQE), which is the number of electron − hole pairs produced by one absorbed photon, is a critical parameter for photodetectors and can be expressed as:

$$EQE = \frac{hcR}{e\lambda} \tag{6}$$

The corresponding calculated EQE are 7.05×10^3 %, 5.54×10^3 %, 7.89×10^3 %, 7.85×10^3 % and 6.48×10^3 %, respectively for photodetectors based on NRs.

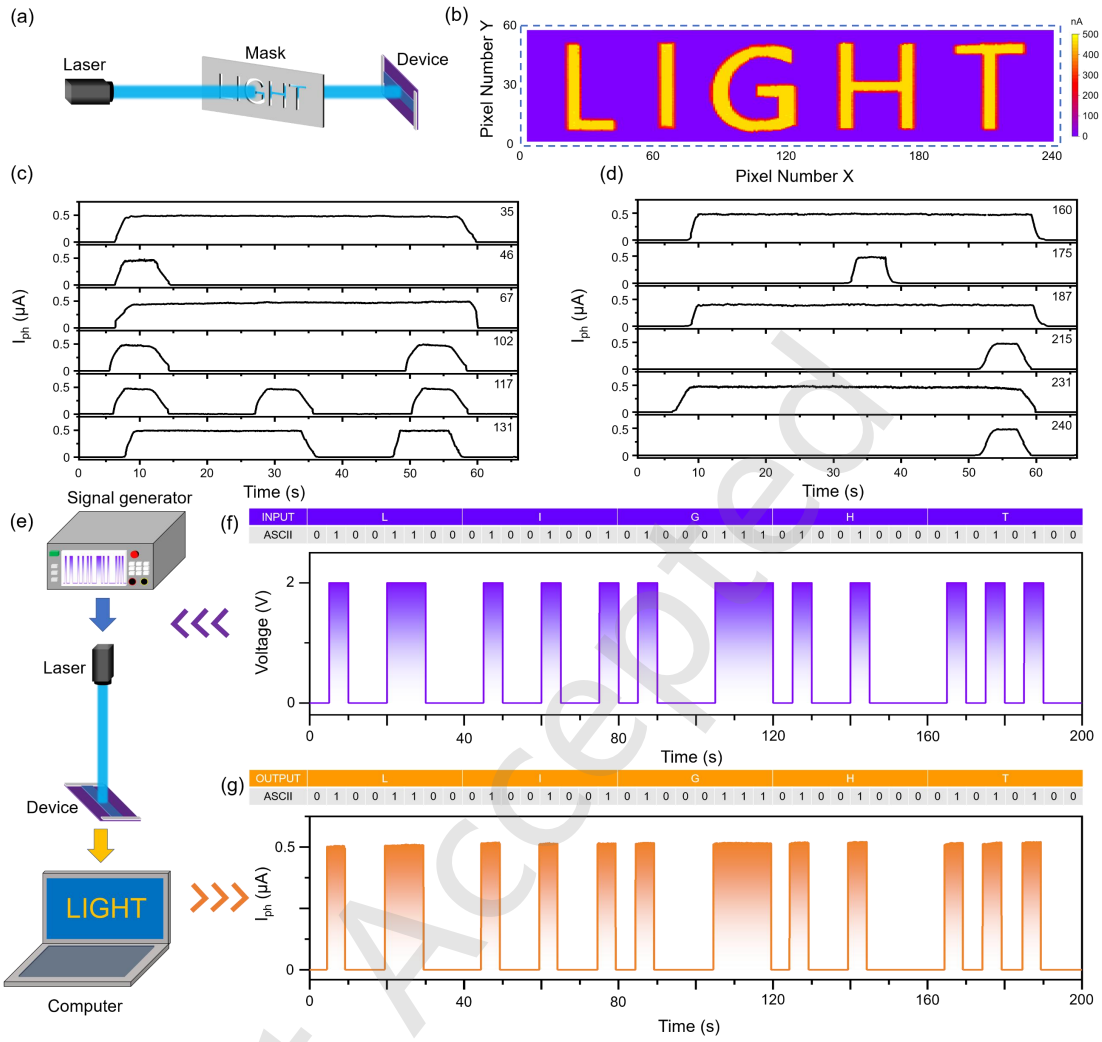

Figure 5. Imaging and optical communication application of the $CsPbCl_3$-based photodetectors. (a) Schematic diagram of the imaging sensing system. (b) Corresponding two-dimensional photocurrent mapping of image "LIGHT" under a 405 nm laser illumination. (c, d) The time-dependent current of "LIGHT" under a 405 nm laser scans along the Y-direction with different X-pixel points. The numbers on the right side indicate the pixel sequences along the X direction. (e) Schematic illustration of the $CsPbCl_3$-based device for an optical communication system. (f) The input signals of the ASCII code "LIGHT". (g) The output photocurrent signals of the ASCII code "LIGHT" by the $CsPbCl_3$-based device.

In consideration of the high photosensitivity of halide perovskites in the visible light region, high-performance photodetectors may have good potential in image-sensing applications. Figure. 5a shows the schematic diagram of the imaging sensing system. A 405 nm laser was used as the light source and placed before the image mask. The mask can be controlled by the stepper motor and moved on the X-Y plane. The real-time spatially resolved light response can be recorded, forming an " LIGHT " image, as shown in Figure. 5b. When a 405 nm light scans along the image mask “LIGHT” along the Y direction with represented X-direction pixel sequences, the time-resolved current of the perovskite NR-based photodetectors are displayed in Figure. 5c and 5d, confirming the high stability and photosensitivity of the imaging system. Figure. 5e shows the schematic of the $CsPbCl_3$-based device in an optical communication system. Using a signal generator, voltage signals representing the ASCII code “LIGHT” were sent to the laser, as shown in Figure. 5f, the laser’s emission can be controlled. After receiving the light signal, the photodetector generated a current signal representing the ASCII code “LIGHT” as shown in Figure. 5g. This signal could be further output and decoded to the information “LIGHT” there by realizing the optical communication. These impressive results of the photodetectors and imaging sensors may show promising future applications in the integrated optoelectronic field.

4 Conclusions

In summary, we developed a source-moving CVD approach to synthesize composition tunable $CsPbCl_{3(1-x)}Br_{3x}$ and $CsPbBr_{3(1-x)}I_{3x}$ (X = 0-1) alloy NRs. Structural characterization of these perovskite structures indicates that the obtained alloyed ribbons have high-quality crystalline. The bandgap of these compositional gradient perovskite alloy NRs can be continuously tuned from 1.7-2.9 eV, with tunable emissions of 417-702 nm, nearly covering the

entire visible light. Moreover, photodetectors based on these NRs show superior detection performances, including high responsivity (37.5 A W^{-1}), high detectivity (2.81×10^{13} Jones), fast response time (16 ~17 ms), as well as high EQE (7×10^{3} %). A high-resolution imaging sensor based on the perovskite NRs has also been demonstrated to identify its good imaging capability. These achievements represent significant advantages in the controllable growth of bandgap tunable perovskite NRs, which may act as effective emission systems and have potential applications in high-performance integrated nanophotonic devices.

Electronic Supplementary Material: Supplementary material (CVD setup, SEM image, EDX spectra, characterization of electrical properties of photodetectors, schematic diagram of confocal microscopy system) is available in the online version of this article at https://doi.org/10.26599/NR.2025.94907347.

Data availability

All data needed to support the conclusions in the paper are presented in the manuscript or the Electronic Supplementary Material. Additional data related to this paper may be requested from the corresponding author upon request.

Acknowledgements

The authors are grateful to the National Natural Science Foundation of China (Nos. 52373246, 62127817, and U23A20380), the National Key Research and Development Program of China (No. 2022YFA1404201), Science and Technology Major Special Project of Shanxi Province (No.

202201010101005), the Shanxi Province Graduate Innovation Project (No. RC2400005577), and the Shanxi Basic Research Program Project (No. 20210302123128) for financial support. The authors acknowledge the assistance of the Instrumental Analysis Center at Taiyuan University of Technology.

Declaration of competing interest

All the contributing authors report no conflict of interests in this work.

Author contribution statement

P. G. and L. X. conceived and designed the research. J. S. W. and X. S. synthesized the perovskite nanoribbons. J. W., X. L., and J. C. H. performed device fabrication and electrical characterizations. J.W. and X. S. contributed to optical characterizations or analysis. J. W., P. G., and L. X. wrote the related discussions. Q. L. participated in the SEM and TEM analysis. P.G., J.W., and L.X. co-wrote the manuscript with all the authors' input. All authors discussed the results and commented on the manuscript.

References

[1] Kim, Y. H.; Cho, H.; Heo, J. H.; Kim, T. S.; Myoung, N. S.; Lee, C. L.; Im, S. H.; Lee, T. W. Light‐Emitting Diodes: Multicolored Organic/Inorganic Hybrid Perovskite Light‐Emitting Diodes. *Adv. Mater.* **2015**, *27*, 1303-1303.

[2] Kim, J. S.; Heo, J. M.; Park, G. S.; Woo, S. J.; Cho, C.; Yun, H. J.; Kim, D. H.; Park, J.; Lee, S. C.; Park, S. H. Ultra-bright, efficient and stable perovskite light-emitting diodes. *Nature*. **2022**, *611*, 688-694.

[3] Cho, H.; Jeong, S. H.; Park, M. H.; Kim, Y. H.; Wolf, C.; Lee, C. L.; Heo, J. H.; Sadhanala, A.; Myoung, N. S.; Yoo, S. Overcoming the electroluminescence efficiency limitations of perovskite light-emitting diodes. *Science*. **2015**, *350*, 1222.

[4] Xiong, Y.; Li, M.; Peng, L.; Thant, A. A.; Wang, N.; Zhu, Y.; Xu, L. Interfaces, Highly Efficient and Stable 2D/3D Heterojunction Perovskite Solar Cells by In Situ Interface Modification with [(p-Fluorophenyl) ethyl] ammonium Acetate. *ACS Appl. Mater. Interfaces*. **2023**, *15*, 15420-15428.

[5] Jiang, J.; Jin, Z.; Gao, F.; Sun, J.; Wang, Q.; Liu, S. $CsPbCl_3$‐Driven Low‐Trap‐Density Perovskite Grain Growth for> 20% Solar Cell Efficiency. *Adv. Sci*. **2018**, *5*, 1800474.

[6] Burschka, J.; Pellet, N.; Moon, S.-J.; Humphry-Baker, R.; Gao, P.; Nazeeruddin, M. K.; Grätzel, M. Sequential deposition as a route to high-performance perovskite-sensitized solar cells. *Nature*. **2013**, *499*, 316-319.

[7] Wang, L.; Liu, J.; Gong, Y.; Yu, J.; Li, Q.; Liu, Z.; Zhang, C.; Wang, S.; Zhang, X.; Yang, X. Efficient, Color-Stable, Pure-Blue Light-Emitting Diodes Based on Aromatic Ligand-Engineered Perovskite Nanoplatelets. *Nano Lett*. **2024**.

[8] Kumawat, N. K.; Tress, W.; Gao, F. Mobile ions determine the luminescence yield of perovskite light-emitting diodes under pulsed operation. *Nat. Commun*. **2021**, *12*, 4899.

[9] Liu, X.-K.; Xu, W.; Bai, S.; Jin, Y.; Wang, J.; Friend, R. H.; Gao, F. Metal halide perovskites for light-emitting diodes. *Nat. Mater*. **2021**, *20*, 10-21.

[10] Fu, Y.; Zhu, H.; Stoumpos, C. C.; Ding, Q.; Wang, J.; Kanatzidis, M. G.; Zhu, X.; Jin, S. Broad wavelength tunable robust lasing from single-crystal nanowires of cesium lead halide perovskites ($CsPbX_3$, X = Cl, Br, I). *ACS Nano.* **2016**, *10*, 7963-7972.

[11] Zhao, C.; Guo, J.; Tao, J.; Chu, J.; Chen, S.; Xing, G., Pulse-doubling perovskite nanowire lasers enabled by phonon-assisted multistep energy funneling. *Light sci.Appl.* **2024**, *13*, 170.

[12] Shang, Q.; Li, M.; Zhao, L.; Chen, D.; Zhang, S.; Chen, S.; Gao, P.; Shen, C.; Xing, J.; Xing, G. Role of the exciton–polariton in a continuous-wave optically pumped $CsPbBr_3$ perovskite laser. *Nano Lett*. **2020**, *20*, 6636-6643.

[13] Zhu, H.; Fu, Y.; Meng, F.; Wu, X.; Gong, Z.; Ding, Q.; Gustafsson, M. V.; Trinh, M. T.; Jin, S.; Zhu, X. Lead halide perovskite nanowire lasers with low lasing thresholds and high quality factors. *Nat. Mater*. **2015**, *14*, 636-642.

[14] Dong, K.; Zhou, H.; Gao, Z.; Xu, M.; Zhang, L.; Zhou, S.; Cui, H.; Wang, S.; Tao, C.; Ke, W. 2D Perovskite Single‐Crystalline Photodetector with Large Linear Dynamic Range for UV Weak‐Light Imaging. *Adv. Funct. Mater*. **2024**, *34*, 2306941.

[15] Zhang, D.; Yang, Y.; Bekenstein, Y.; Yu, Y.; Gibson, N. A.; Wong, A. B.; Eaton, S. W.; Kornienko, N.; Kong, Q.; Lai, M. Synthesis of composition tunable and highly luminescent cesium lead halide nanowires through anion-exchange reactions. *J. Am. Chem. Soc.* **2016**, *138*, 7236-7239.

[16] Meng, Y.; Zhang, Y.; Lai, Z.; Wang, W.; Wang, W.; Li, Y.; Li, D.; Xie, P.; Yin, D.; Chen, D. Au-seeded $CsPbI_3$ nanowire optoelectronics via exothermic nucleation. *Nano Lett*. **2022**, *23*, 812-819.

[17] Meng, Y.; Lan, C.; Li, F.; Yip, S.; Wei, R.; Kang, X.; Bu, X.; Dong, R.; Zhang, H.; Ho, J. C. Direct vapor–liquid–solid synthesis of all-inorganic perovskite nanowires for high-performance electronics and optoelectronics. *ACS Nano*. **2019**, *13*, 6060-6070.

[18] Bao, Y.; Wang, H.; An, M.; Tang, H.; Li, J.; Li, J.; Tan, C.; Luo, Y.; Xu, J.; Yang, Y. Defect-modulated synthesis and optoelectronic properties in chemical vapor deposited $CsPbBr_3$ microplates. *Nano Res*. **2024**, *17*, 4610-4615.

[19] Yu, Y.; Xia, X.; Xu, C.; Lv, Z.; Wang, X.; Liao, L. Customizable Organic Charge-Transfer Cocrystals for the Dual-Mode Optoelectronics in the NIR (II) Window. *J. Am. Chem. Soc.* **2024**, *146*, 11845-11854.

[20] Lv, Q.; Wang , X.; Yu, Y.; Xu, C.; Yu, Y.; Xia, X.; Zheng , M.; Liao, L. Lateral epitaxial growth of two-dimensional organic heterostructures. *Nat. Chem.* **2024**, *16*, 201-209.

[21] Ning, C. Z.; Dou, L.; Yang, P. Bandgap engineering in semiconductor alloy nanomaterials with widely tunable compositions. *Nat. Rev. Mater*. **2017**, *2*, 1-14.

[22] Fan, J.; Guo, P.; Lv, Q.; Shen, X.; Song, X.; Meng, Y.; Xu, Z.; Wang, J.; Xu, T.; Li, X. Bandgap-Engineered $CsPbBr_{3x}I_{3-3x}$ Alloy Nanowires for Broadly Tunable Nanoscale Lasers. *ACS Appl. Nano Mater*. **2023**, *6*, 17881-17889.

[23] Brenner, P.; Glöckler, T.; Rueda-Delgado, D.; Abzieher, T.; Lemmer, U. Triple cation mixed-halide perovskites for tunable lasers. *Opt. Mater. Express*. **2017**, *7*, 4082.

[24] Nedelcu, G.; Protesescu, L.; Yakunin, S.; Bodnarchuk, M. I.; Grotevent, M. J.; Kovalenko, M. V. Fast Anion-Exchange in Highly Luminescent Nanocrystals of Cesium Lead Halide Perovskites ($CsPbX_3$, X = Cl, Br, I). *Nano Lett*. **2015**, *18*, 5635-5640.

[25] Pan, D.; Fu, Y.; Chen, J.; Czech, K. J.; Wright, J. C.; Jin, S. Visualization and Studies of Ion Diffusion Kinetics in Cesium Lead Bromide Perovskite Nanowires. *Nano Lett*. **2018**, *21*, 5564-5571.

[26] Cen, G.; Xia, Y.; Zhao, C.; Fu, Y.; An, Y.; Yuan, Y.; Shi, T.; Mai, W. Precise Phase Control of Large-Scale Inorganic Perovskites via Vapor-Phase Anion-Exchange Strategy. *Small* **2020**, *16*, 2005226.

[27] Tian, W.; Leng, J.; Zhao, C.; Jin, S. Long-Distance Charge Carrier Funneling in Perovskite Nanowires Enabled by Built-in Halide Gradient. *J. Am. Chem. Soc.* **2017**, *139*, 579-582.

[28] Dou, L.; Lai, M.; Kley, C. S.; Yang, Y.; Yang, P. Spatially resolved multicolor $CsPbX_3$ nanowire heterojunctions via anion exchange. *P. Natl. Acad. Sci. USA*. **2017**, *114*, 201703860.

[29] Fu, Y.; Poddar, S.; Ren, B.; Xie, Y.; Zhang, Q.; Zhang, D.; Cao, B.; Tang, Y.; Ding, Y.; Qiu, X. Strongly Quantum-Confined Perovskite Nanowire Arrays for Color-Tunable Blue-Light-Emitting Diodes. *ACS Nano*. **2022**, *16*, 8388-8398.

[30] Massasa, E. H.; Strassberg, R.; Vurgaft, A.; Kauffmann, Y.; Cohen, N.; Bekenstein, Y. Thin Layer Buckling in Perovskite $CsPbBr_3$ Nanobelts. *Nano Lett*. **2021**, *21*, 5564-5571.

[31] Tang, B.; Hu, Y.; Lu, J.; Dong, H.; Mou, N.; Gao, X.; Wang, H.; Jiang, X.; Zhang, L. Energy transfer and wavelength tunable lasing of single perovskite alloy nanowire. *Nano Energy*. **2020**, 71, 104641.

[32] Li, J.; Xu, J.; Bao, Y.; Li, J.; Wang, H.; He, C.; An, M.; Tang, H.; Sun, Z.; Fang, Y.; Liang, S.; Yang, Y. Anion-Exchange Driven Phase Transition in $CsPbI_3$ Nanowires for Fabricating Epitaxial Perovskite Heterojunctions. *Adv. Mater*. **2022**, *34*, 2109867.

[33] He, X.; Liu, P.; Zhang, H.; Liao, Q.; Yao, J.; Fu, H. Patterning Multicolored Microdisk Laser Arrays of Cesium Lead Halide Perovskite. *Adv. Mater.* **2017**, *29*, 1604510.

[34] Tang, X.; Zhou, H.; Pan, X.; Liu, R.; Wu, D.; Wang, H.. All-Inorganic Halide Perovskite Alloy Nanowire Network Photodetectors with High Performance. *ACS Appl. Mater. Interfaces*. **2020**, *12*, 4843-4848.

[35] Guo, P.; Hu, W.; Zhang, Q.; Zhuang, X.; Zhu, X.; Zhou, H.; Shan, Z.; Xu, J.; Pan, A. Semiconductor Alloy Nanoribbon Lateral Heterostructures for High-Performance Photodetectors. *Adv. Mater.* **2014**, *26*, 2844-2849.

[36] Hu, L.; Yan, J.; Liao, M.; Xiang, H.; Gong, X.; Zhang, L.; Fang, X. An optimized ultraviolet‐a light photodetector with wide‐range photoresponse based on ZnS/ZnO biaxial nanobelt. *Adv. Mater*. **2012**, *24*, 2305-2309.

[37] Xu, J.; Ma, L.; Guo, P.; Zhuang, X.; Pan, A. Room-Temperature Dual-Wavelength Lasing from Single-Nanoribbon Lateral Heterostructures. *J. Am. Chem. Soc*. **2012**, *134*, 12394-12397.

[38] Zhuang, X.; Guo, P.; Zhang, Q.; Liu, H.; Li, D.; Hu, W.; Zhu, X.; Zhou, H.; Pan, A. Lateral composition-graded semiconductor nanoribbons for multi-color nanolasers. *Nano Res*. **2016**, 4, 9.

[39] Guo, P.; Hossain, M. K.; Shen, X.; Sun, H.; Yang, W.; Liu, C.; Ho, C. Y.; Kwok, C. K.; Tsang, S. W.; Luo, Y. Room‐Temperature Red‐Green‐Blue Whispering‐Gallery Mode Lasing and White‐Light Emission from Cesium Lead Halide Perovskite ($CsPbX_3$, X = Cl, Br, I) Microstructures. *Adv. Opt. Mater*. **2018**, *6*, 1700993.

[40] Wang, Y.; Guan, X.; Li, D.; Cheng, H.-C.; Duan, X.; Lin, Z.; Duan, X. Chemical vapor deposition growth of single-crystalline cesium lead halide microplatelets and heterostructures for optoelectronic applications. *Nano Res*. **2017**, *10*, 1223-1233.

[41] Hossain, M. K.; Guo, P.; Qarony, W.; Tsang, Y. H.; Liu, C.; Tsang, S. W.; Ho, J. C.; Yu, K. M. Controllable optical emission wavelength in all-inorganic halide perovskite alloy microplates grown by two-step chemical vapor deposition. *Nano Res*. **2020**, *13*, 2939-2949.

[42] Mukhtar, M.; Bibi, S.; Erten Ela, S.; Yavuz, C.; Mubeen, M.; Sumreen, P.; Khalid, M. A.; Ul-Hamid, A.; Iqbal, A. Photon-induced electron transfer in ligand-stabilized monoclinic $CsPbBr_3$ and alanine-functionalized graphene heterostructures. *J. Phys. Chem. C*. **2022**, *126*, 15298-15308.

[43] Wang, S.; Shen, W.; Chu, Y.; Zhang, W.; Hong, L.; Mei, A.; Rong, Y.; Tang, Y.; Hu, Y.; Han, H. Mesoporous-carbon-based fully-printable all-inorganic monoclinic CsPbBr3 perovskite solar cells with ultrastability under high temperature and high humidity. *J. Phys. Chem. Lett*. **2020**, *11*, 9689-9695.

[44] Protesescu, L.; Yakunin, S.; Bodnarchuk, M. I.; Krieg, F.; Caputo, R.; Hendon, C. H.; Yang, R. X.; Walsh, A.; Kovalenko, M. V. Nanocrystals of cesium lead halide perovskites ($CsPbX_3$, X = Cl, Br, and I): novel optoelectronic materials showing bright emission with wide color gamut. *Nano Lett*. **2015**, *15*, 3692-3696.

[45] Zhang, Q.; Su, R.; Liu, X.; Xing, J.; Sum, T. C.; Xiong, Q. High‐quality whispering‐gallery‐mode lasing from cesium lead halide perovskite nanoplatelets. *Adv. Funct. Mater.* **2016**, *26*, 6238-6245.

[46] Zhang, Y.; Lu, D.; Gao, M.; Lai, M.; Lin, J.; Lei, T.; Lin, Z.; Quan, L. N.; Yang, P. Quantitative imaging of anion exchange kinetics in halide perovskites. *P. Natl. Acad. Sci. USA*. **2019**, *116*, 12648-12653.

[47] Zhou, Y.; Zhou, Z.; Chen, M.; Zong, Y.; Huang, J.; Pang, S.; Padture, N. P. Doping and alloying for improved perovskite solar cells. *J. Mater. Chem. A*. **2016**, *4*, 17623-17635.

[48] Wu, W.; Han, X.; Li, J.; Wang, X.; Zhang, Y.; Huo, Z.; Chen, Q.; Sun, X.; Xu, Z.; Tan, Y. Ultrathin and conformable lead halide perovskite photodetector arrays for potential application in retina‐like vision sensing. *Adv. Mater*. **2021**, *33*, 2006006.

[49] Xu, Z.; Pan, X.; Lu, H.; Lu, Q.; Liang, Y.; He, Z.; Zhu, Y.; Yu, Y.; Wu, W.; Han, X. Surface Energy‐Assisted Patterning of Vapor Deposited All‐Inorganic Perovskite Arrays for Wearable Optoelectronics. *Adv. Sci*. **2024**, 2402635.

[50] Zhang, Y.; Yang, X.; Dai, Y.; Yu, W.; Yang, L.; Zhang, J.; Yu, Q.; Dong, Z.; Huang, L.; Chen, C. Ternary $GePdS_3$: 1D van der Waals Nanowires for Integration of High-Performance Flexible Photodetectors. *ACS Nano*. **2023**, *17*, 8743-8754.

[51] Lv, Q.; Shen, X.; Li, X.; Meng, Y.; Yu, K. M.; Guo, P.; Xiao, L.; Ho, J. C.; Duan, X.; Duan, X. On-Wire Design of Axial Periodic Halide Perovskite Superlattices for High-Performance Photodetection. *ACS Nano*. **2024**, *18*, 18022-18035.

Electronic Supplementary Material

Bandgap engineering of halide perovskite nanoribbons for high-performance photodetection

Pengfei Guo[1,2,*], Jishen Wang[1], Xia Shen[1], Qihang Lv[1], Xuyang Li[1], Zitong Xu[1], Shuangping Han[1], Yaoxing Bian[1], You Meng[4], Lingzhen Yang[1], Chengbing Qin[3], Kin Man Yu[6,7], Johnny C. Ho[2,5], and Liantuan Xiao[1,*]

[1]College of Physics and Optoelectronics, Taiyuan University of Technology, Taiyuan 030024, China

[2]Department of Materials Science and Engineering, City University of Hong Kong, Kowloon, Hong Kong 999077, China

[3]State Key Laboratory of Quantum Optics and Quantum Optics Devices, Institute of Laser Spectroscopy, Shanxi University, Taiyuan 030024, China

[4]Changsha Semiconductor Technology and Application Innovation Research Institute, College of Semiconductors (College of Integrated Circuits), Hunan University, Changsha 410082 China

[5]Institute for Materials Chemistry and Engineering, Kyushu University, Fukuoka 8819-0395, Japan

[6]Department of Physics, “National Sun Yat Sen University”, Kaohsiung, Taiwan 80424, China

[7]Materials Sciences Division, Lawrence Berkeley National Laboratory, CA 94720, USA

✉Address correspondence to Pengfei Guo, guopengfei2010@126.com; Liantuan Xiao, xlt@sxu.edu.cn

Supporting information to https://doi.org/10.26599/NR.2025.94907347

(a)

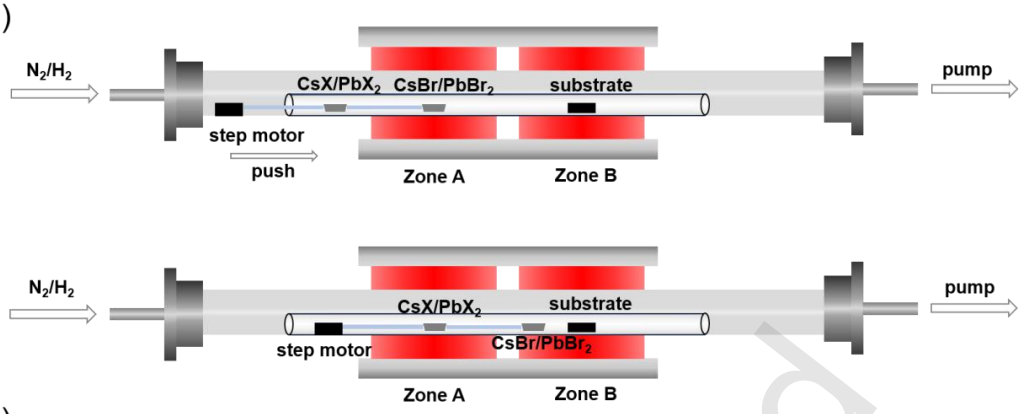

(b)

T (℃) \ t (min) / x (I)	0	20	30	40	60	100
420	0	0.2	0.34	0.48	0.65	1

(c)

T (℃) \ t (min) / x (Cl)	0	10	30	60	90
440	0	0.37	0.56	0.78	1

Figure. S1. (a) Schematic diagram of the experiment setup. (b, c) Relationship between x (composition ratio of Cl or I in $CsPbX_3$ alloy NRs) and the growth temperature and growth time of the anion exchange process.

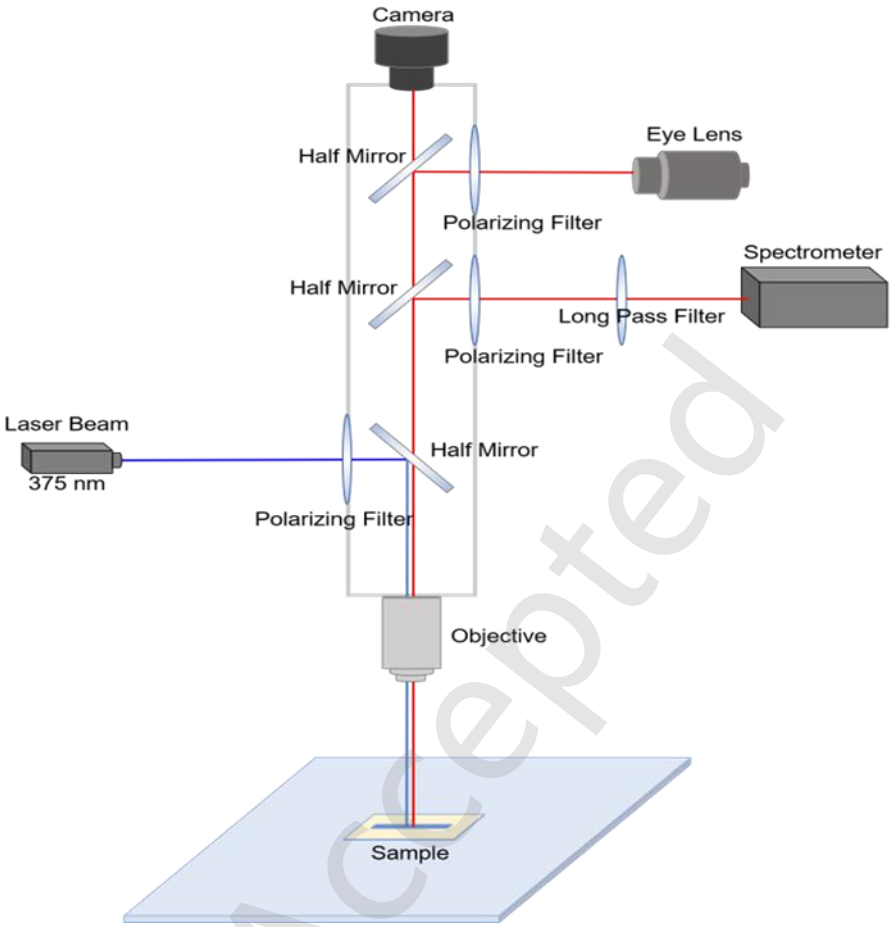

Figure. S2. Schematic diagram of the confocal optical system for optical measurement.

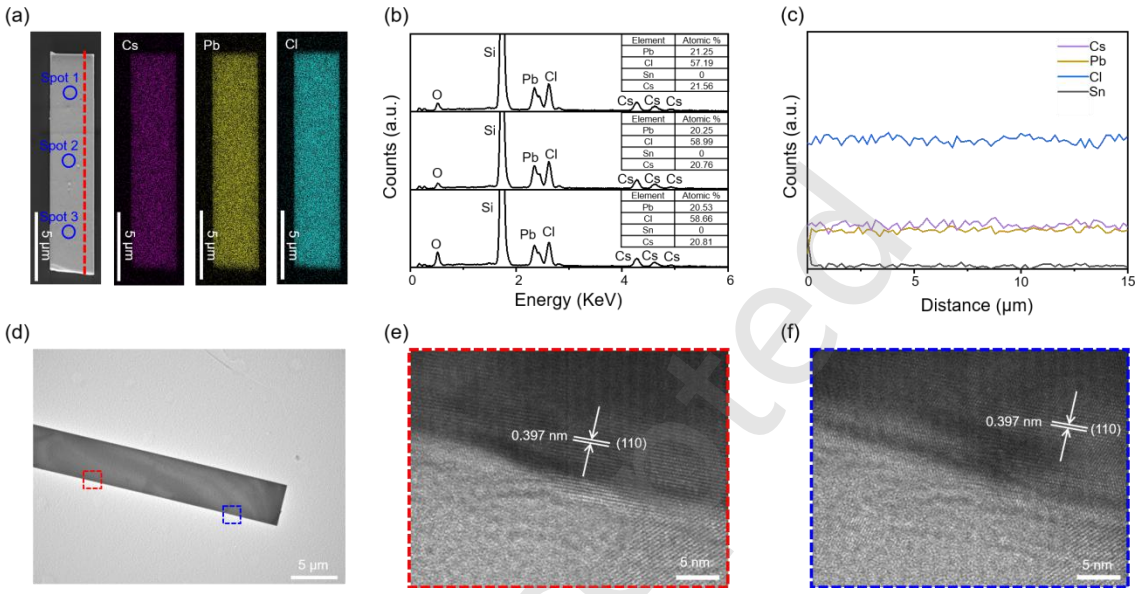

Figure. S3. Structural characterization of $CsPbCl_3$ NRs. (a) SEM images and EDX element mapping of typical $CsPbCl_3$ NR. (b) The EDX element scanning profile of a single nanobelt at Spot 1, Spot 2, and Spot 3. (c) Line scanning EDX profile of the NRs along the axial direction. (d) Low-resolution TEM images of a typical NR. (e, f) High-resolution TEM images of two typical positions along the NR.

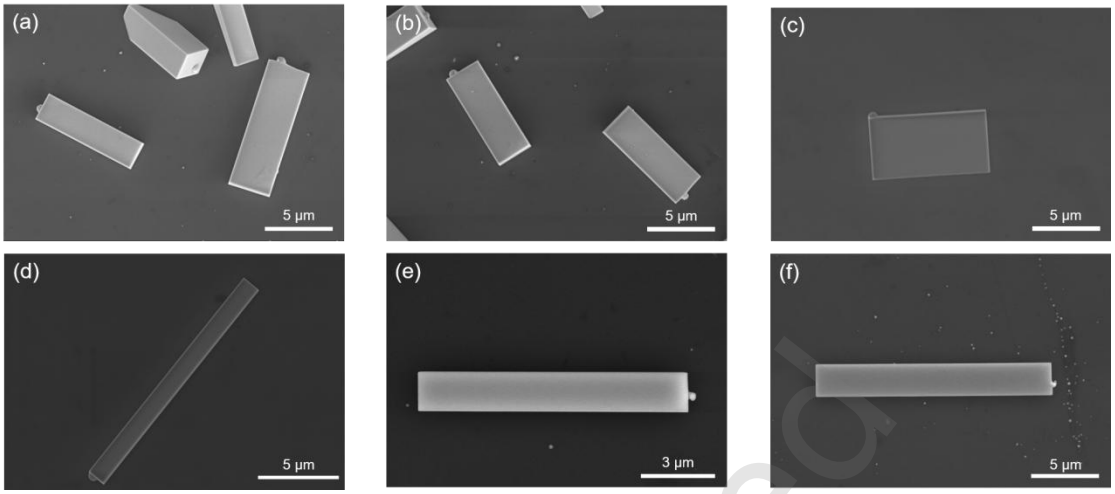

Figure. S4. (a-f) SEM images of some typical $CsPbBr_3$ NRs on Si/SiO_2 substrate.

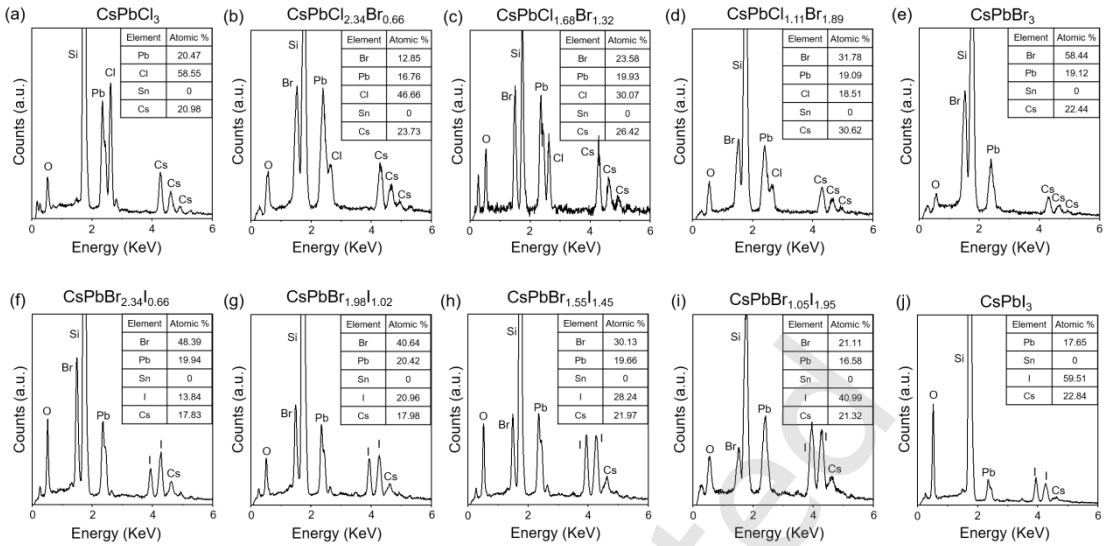

Figure. S5. (a-j) EDX spectra of perovskite $CsPbCl_{3(1-x)}Br_{3x}$ and $CsPbBr_{3(1-x)}I_{3x}$ (X = 0-1) alloy NRs with different compositions.

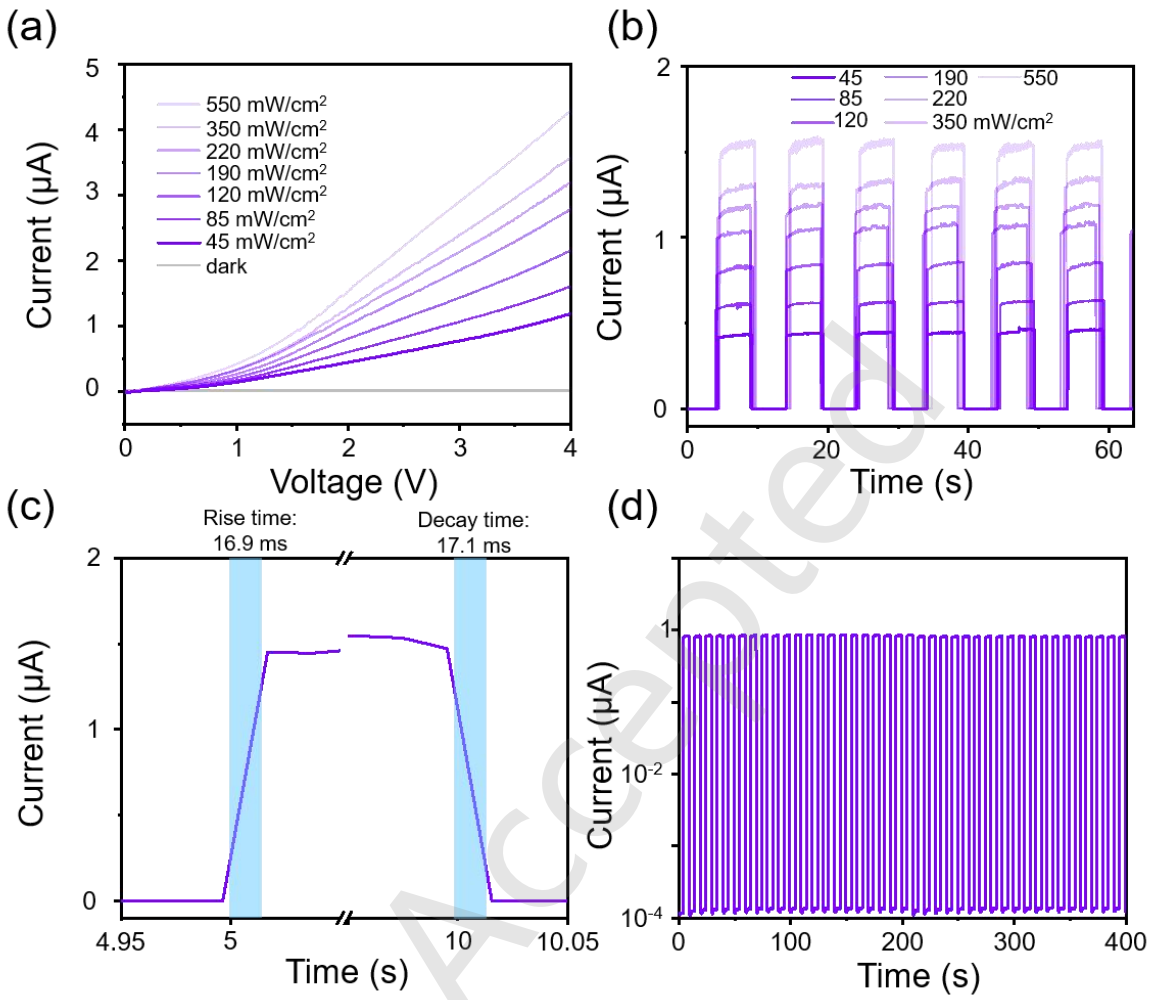

Figure. S6. Electrical performance of $CsPbCl_3$ nanoribbon photodetectors: (a) The I-V curve of the device under 405 nm laser irradiation in optical power intensity between 0-550 mW/cm^2. (b) The I-T curve of the device under 2V bias and 405 nm laser irradiation, the optical power intensity ranging from 45-550 mW/cm^2. (c) Response time of photodetector under 405 nm laser irradiation. (d) The I-T curve is a function of time under the chopped light illumination of 70 mW/cm^2 and a 2 V bias.

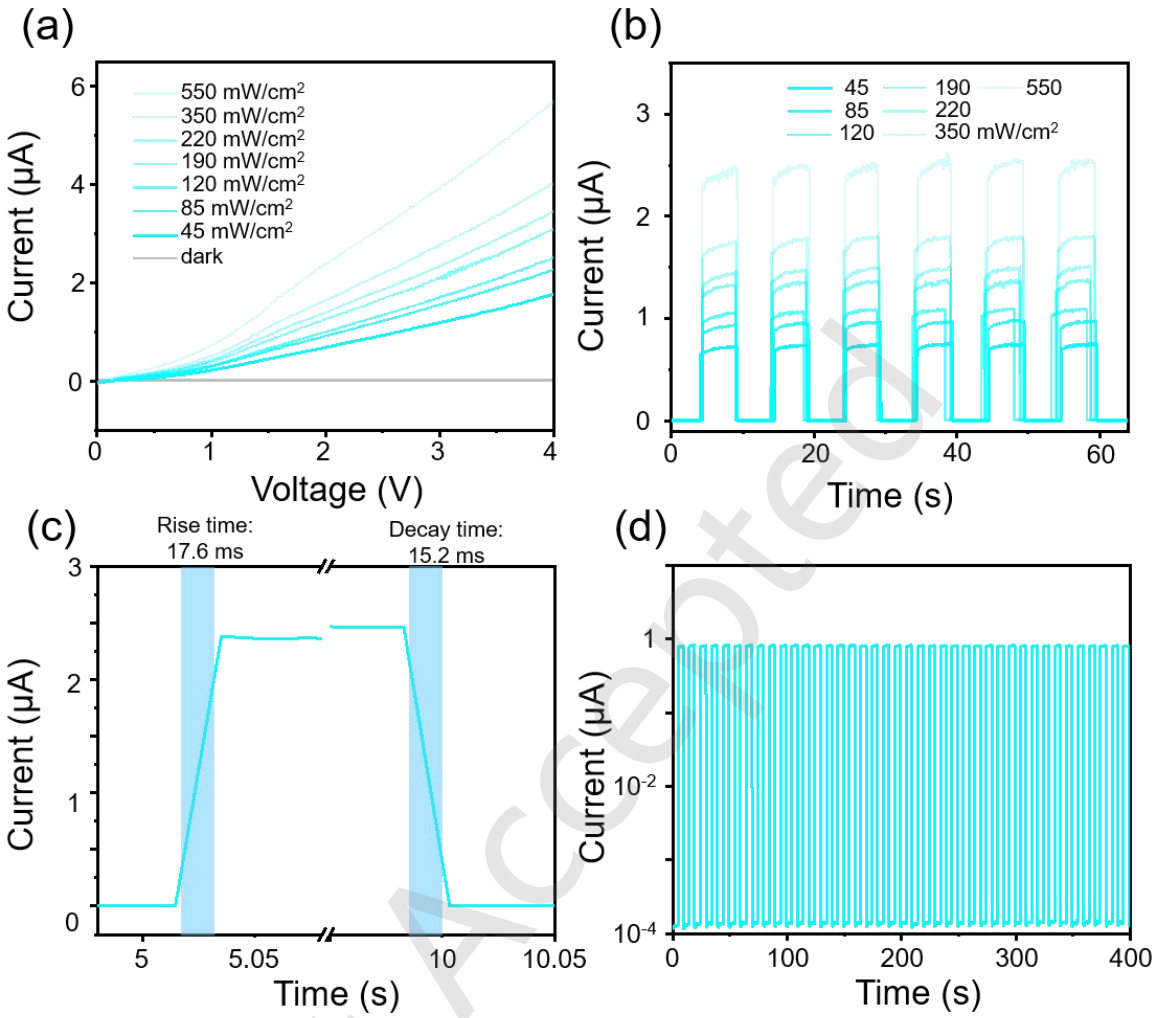

Figure. S7. Electrical performance of $CsPbCl_{1.68}Br_{1.32}$ nanoribbon photodetectors: (a) The I-V curve of the device under 450 nm laser irradiation in optical power intensity between 0-550 mW/cm^2. (b) The I-T curve of the device under 2V bias and 450 nm laser irradiation, the optical power intensity ranging from 45-550 mW/cm^2. (c) Response time of photodetector under 450 nm laser irradiation. (d) The I-T curve is a function of time under the chopped light illumination of 70 mW/cm^2 and a 2 V bias.

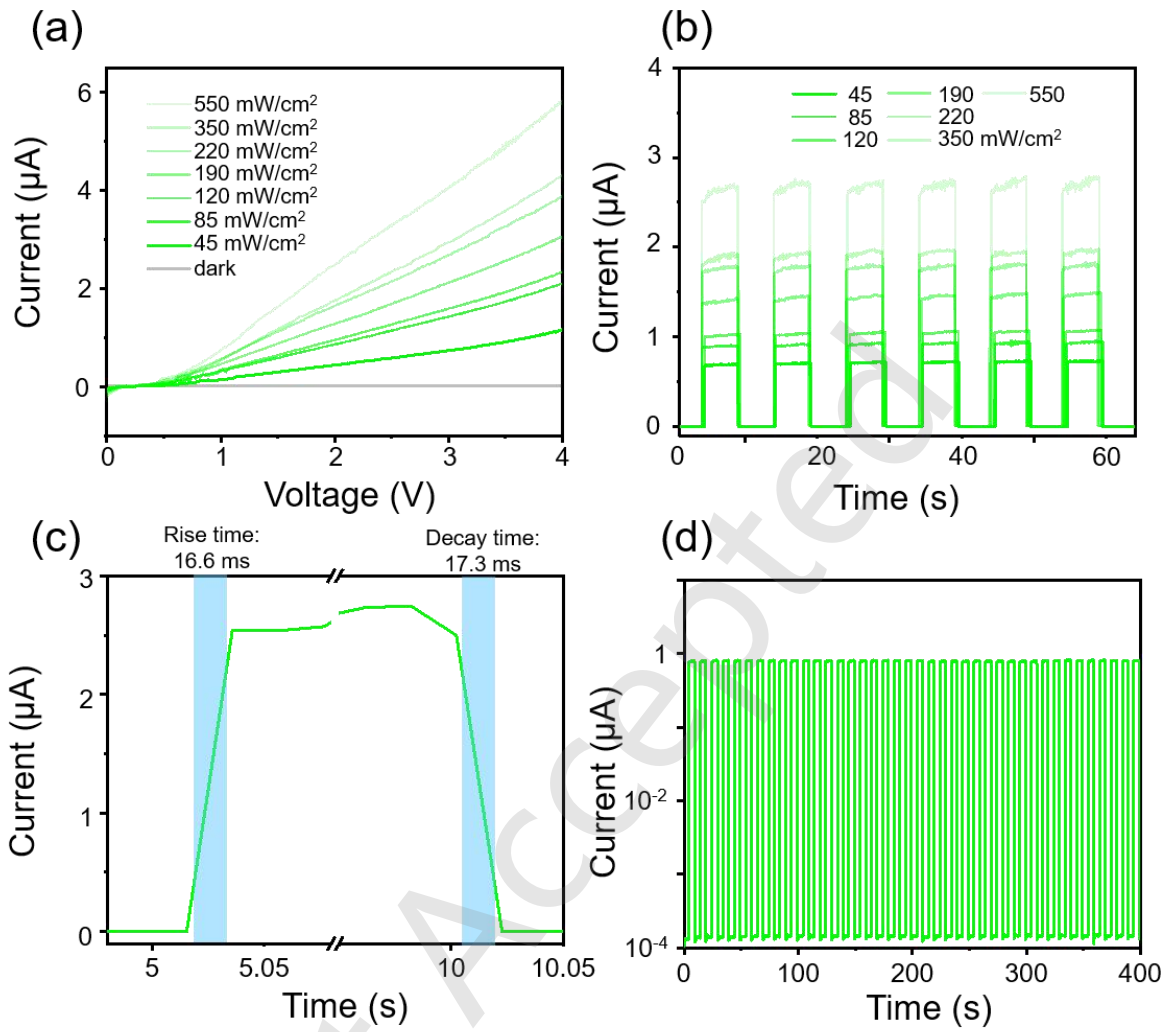

Figure. S8. Photoelectrical performance of $CsPbBr_3$ nanoribbon photodetectors: (a) The I-V curve of the device under 520 nm laser irradiation in optical power intensity between 0-550 mW/cm^2. (b) The I-T curve of the device under 2V bias and 520 nm laser irradiation, the optical power intensity ranging from 45-550 mW/cm^2. (c) Response time of photodetector under 520 nm laser irradiation. (d) The I-T curve is a function of time under the chopped light illumination of 70 mW/cm^2 and a 2 V bias.

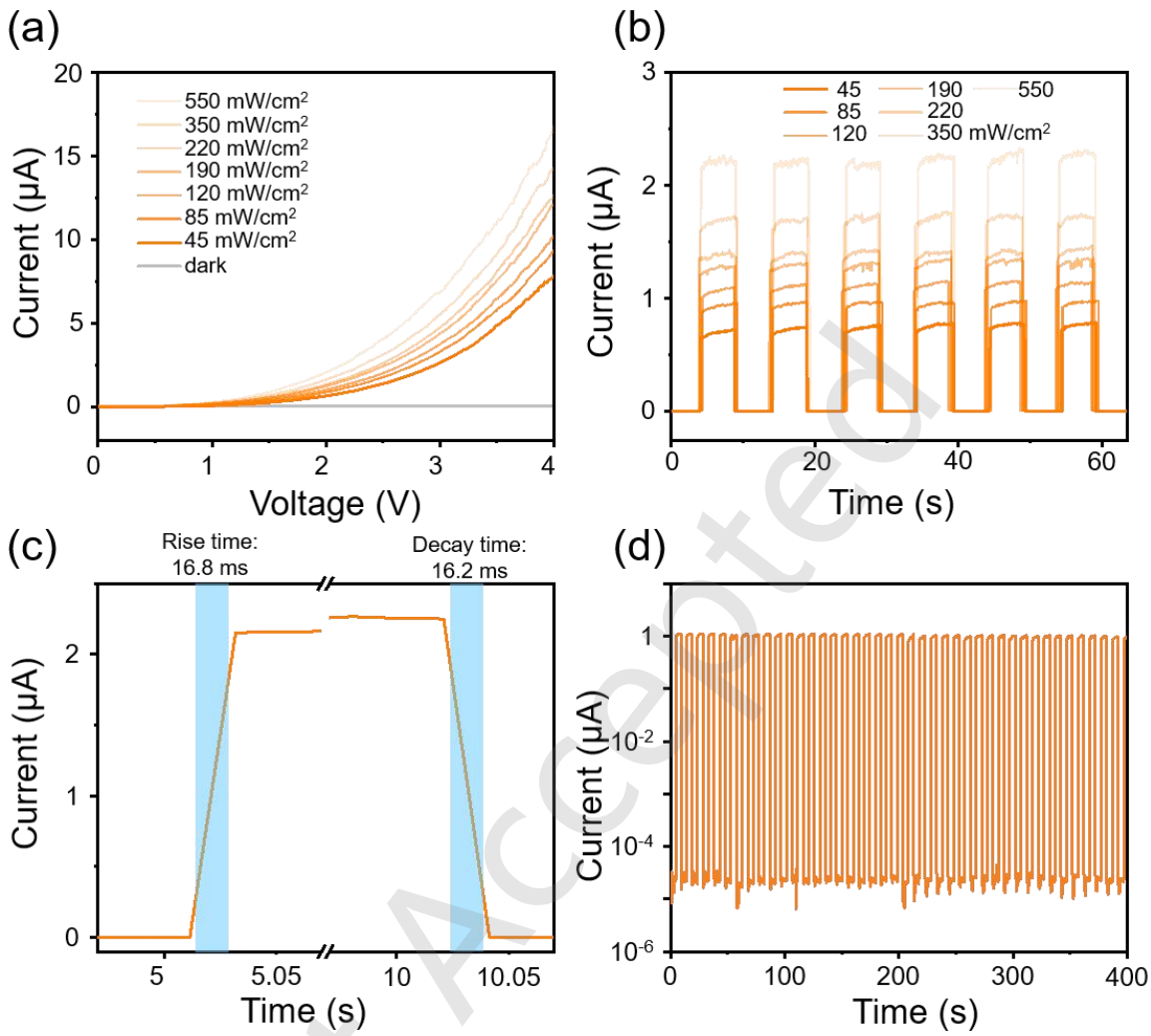

Figure. S9. Electrical performance of $CsPbBr_{1.32}I_{1.68}$ nanoribbon photodetectors: (a) The I-V curve of the device under 638 nm laser irradiation in optical power intensity between 0-550 mW/cm^2. (b) The I-T curve of the device under 2V bias and 638 nm laser irradiation, the optical power intensity ranging from 45-550 mW/cm^2. (c) Response time of photodetector under 638 nm laser irradiation. (d) The I-T curve is a function of time under the chopped light illumination of 70 mW/cm^2 and a 2 V bias.

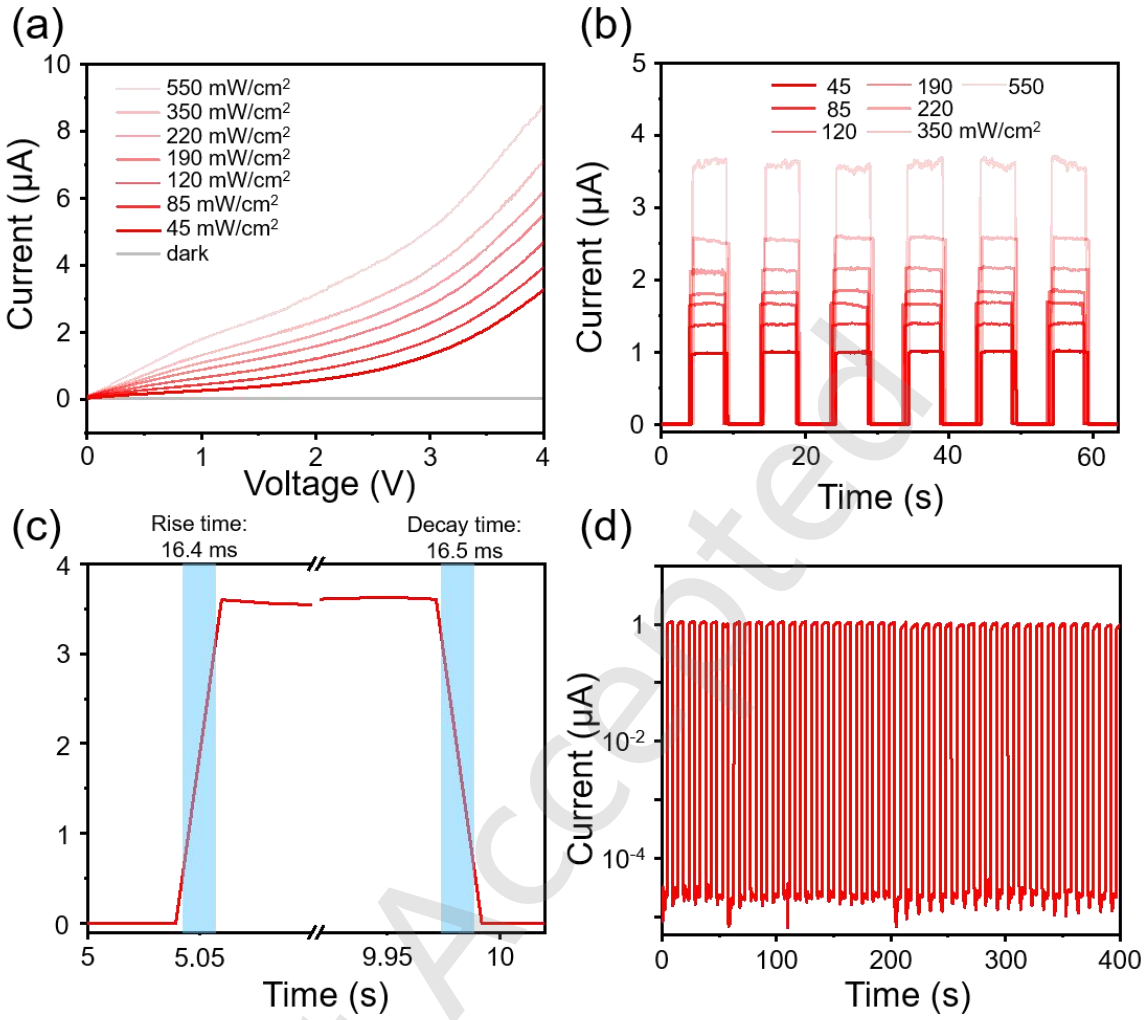

Figure. S10. Electrical performance of $CsPbBr_{0.44}I_{2.56}$ nanoribbon photodetectors: (a) The I-V curve of the device under 660 nm laser irradiation in optical power intensity between 0-550 mW/cm^2. (b) The I-T curve of the device under 2V bias and 660 nm laser irradiation, the optical power intensity ranging from 30-550 mW/cm^2. (c) Response time of photodetector under 660 nm laser irradiation. (d) The I-T curve is a function of time under the chopped light illumination of 70 mW/cm^2 and a 2 V bias.

Table S1. Synthesis of photodetectors based on perovskite nanomaterials.

Materials	Channel	R (A/W)	D* ($\times 10^{12}$ Jones)	Rise time (ms)	Decay time (ms)	On/off ratio	Refs.
$CsPbBr_3$	Microparticles	0.18	0.61	1.8	1.0		[1]
$CsPbBr_3$	Microcrystals	0.172	4.8	0.14	0.12	1.3×10^5	[2]
$MAPbI_3$	Microcrystals	275	10	0.03	0.02		[3]
$CsPbI_3$	Single NW	4.49×10^3	7.9	<50	<50	10^4–10^5	[4]
$CsPbI_3$	NW arrays	0.35	0.0164				[5]
$MAPbI_3$	NWs	1.32	2.5	0.2	0.3		[6]
$MAPbI_3$	NW Network	0.23	0.7	53.2	50.2		[7]
$MAPbI_3$	NW Network	0.1	1.02	0.3	0.4	340	[8]
$CsPbCl_3$	Single microplatelet	0.45	0.1	8	7		[9]
$Cs_3Bi_2I_9$	2D layered crystal	0.033	0.01	10.2	37.2	40	[10]
$MAPbI_3$	MWs array	13.57	5.25	0.08	0.24	>100	[11]
$MAPbI_3$	NWs array	410	9.1	0.22	0.79	>100	[12]
$CsPbCl_3$	NWs	0.398	0.33	24	25	2×10^5	[13]
$CsPbBr_3$	NWs array	7.66	4.05	275	550	10^3	[14]
$CsPbBr_3$	NWs	2.36×10^{-3}	6.17	3	2.8	2.957×10^3	[15]
$MAPbI_3$	MWs Arrays	69.11	8.6	0.81	0.77	2.1×10^3	[16]
$MAPbBr_3$	MWs Array	20	0.41	1.6	6.4	$>10^5$	[17]
$MAPbI_3$	NWs	4.95	20	<0.1	<0.1	4×10^3	[18]
$MASnI_3$	NWs	0.47	0.088	1500	400	5	[19]
$MAPbI_3$	NWs	0.16	1.3	0.0138	0.0161	3.3×10^4	[20]
$MAPbI_3$	NWs Arrays	0.012	7.3	0.088	0.154	$>10^4$	[21]
$CsPbBr_3$	NWs	0.3	10	0.4	0.43	10^6	[22]

$CsPbBr_3$	MWs	118	>1	<40	<40	＞100	[23]
$CsPbBr_3$	MWs Arrays	1.9	0.14				[24]
$(PA)_2PbBr_4$	microplatelet	2.22	23	1.59	1.66	$>10^3$	[25]
CsPbBr3	microplates	80	0.05	1	1		[26]
$FASnI_3$-CNI	films	0.37	9.12	0. 391μs	0. 391μs		[27]
$CsPbBr_3$	films	11.56	38.3	0.81	2.03	13 887,	[28]
$CsPbX_3$	nanoribbons	37.5	28.1	16	16	$>10^5$	This work

REFERENCES

[1] Li, X.; Yu, D.; Cao, F.; Gu, Y.; Wei, Y.; Wu, Y.; Song, J.; Zeng, H. Healing all‐inorganic perovskite films via recyclable dissolution‐recyrstallization for compact and smooth carrier channels of optoelectronic devices with high stability. *Adv. Funct. Mater.* **2016**, *26*, 5903-5912.

[2] Zhou, H.; Zeng, J.; Song, Z.; Grice, C. R.; Chen, C.; Song, Z.; Zhao, D.; Wang, H.; Yan, Y. Self-powered all-inorganic perovskite microcrystal photodetectors with high detectivity. *J. Phys. Chem. Lett.* **2018**, *9*, 2043-2048.

[3] Saidaminov, M. I.; Haque, M. A.; Savoie, M.; Abdelhady, A. L.; Cho, N.; Dursun, I.; Buttner, U.; Alarousu, E.; Wu, T.; Bakr, O. M. Perovskite photodetectors operating in both narrowband and broadband regimes. *Adv. Mater.* **2016**, *28*, 8144-8149.

[4] Meng, Y.; Lan, C.; Li, F.; Yip, S.; Wei, R.; Kang, X.; Bu, X.; Dong, R.; Zhang, H.; Ho, J. C. Direct vapor–liquid–solid synthesis of all-inorganic perovskite nanowires for high-performance electronics and optoelectronics. *ACS Nano* **2019**, *13*, 6060-6070.

[5] Zhou, Y.; Luo, J.; Zhao, Y.; Ge, C.; Wang, C.; Gao, L.; Zhang, C.; Hu, M.; Niu, G.; Tang, J. Flexible linearly polarized photodetectors based on all‐inorganic perovskite $CsPbI_3$ nanowires. *Adv. Opt. Mater.* **2018**, *6*, 1800679.

[6] Deng, H.; Dong, D.; Qiao, K.; Bu, L.; Li, B.; Yang, D.; Wang, H.-E.; Cheng, Y.; Zhao, Z.; Tang, J. Growth, patterning and alignment of organolead iodide perovskite nanowires for optoelectronic devices. *Nanoscale.* **2015**, *7*, 4163-4170.

[7] Asuo, I. M.; Gedamu, D.; Ka, I.; Gerlein, L. F.; Fortier, F.-X.; Pignolet, A.; Cloutier, S. G.;

Nechache, R. High-performance pseudo-halide perovskite nanowire networks for stable and fast-response photodetector. *Nano Energy.* **2018**, *51*, 324-332.

[8] Deng, H.; Yang, X.; Dong, D.; Li, B.; Yang, D.; Yuan, S.; Qiao, K.; Cheng, Y.-B.; Tang, J.; Song, H. Flexible and semitransparent organolead triiodide perovskite network photodetector arrays with high stability. *Nano Lett.* **2015**, *15*, 7963-7969.

[9] Chen, M.; Zou, Y.; Wu, L.; Pan, Q.; Yang, D.; Hu, H.; Tan, Y.; Zhong, Q.; Xu, Y.; Liu, H. Solvothermal synthesis of high ‐ quality all ‐ inorganic cesium lead halide perovskite nanocrystals: from nanocube to ultrathin nanowire. *Adv. Funct. Mater.* **2017**, *27*, 1701121.

[10] Qi, Z.; Fu, X.; Yang, T.; Li, D.; Fan, P.; Li, H.; Jiang, F.; Li, L.; Luo, Z.; Zhuang, X. Highly stable lead-free $Cs_3Bi_2I_9$ perovskite nanoplates for photodetection applications. *Nano Res.* **2019**, *12*, 1894.-1899.

[11] Deng, W.; Zhang, X.; Huang, L.; Xu, X.; Wang, L.; Wang, J.; Shang, Q.; Lee, S.-T.; Jie, J. Aligned Single-Crystalline Perovskite Microwire Arrays for High-Performance Flexible Image Sensors with Long-Term Stability. *Adv. Mater.* **2016**, *28*, 2201-2208.

[12] Zhou, Q.; Park, J. G.; Nie, R.; Thokchom, A. K.; Ha, D.; Pan, J.; Seok, S. I.; Kim, T. Nanochannel-assisted perovskite nanowires: from growth mechanisms to photodetector applications. *ACS Nano.* **2018**, *12*, 8406-8414.

[13] Wu, X.; Sun, J.; Shao, H.; Zhai, Y.; Li, L.; Chen, W.; Zhu, J.; Dong, B.; Xu, L.; Zhou, D. Self-powered UV photodetectors based on $CsPbCl_3$ nanowires enabled by the synergistic effect of acetate and lanthanide ion passivation. *Chem. Eng. J.* **2021**, *426*, 131310.

[14] Tong, G.; Jiang, M.; Son, D. Y.; Ono, L. K.; Qi, Y. 2D Derivative Phase Induced Growth of 3D all inorganic perovskite micro–nanowire array based photodetectors. *Adv. Funct. Mater.* **2020**, *30*, 2002526.

[15] Yu, M.; Zhang, D.; Xu, Y.; Lin, J.; Yu, C.; Fang, Y.; Liu, Z.; Guo, Z.; Tang, C.; Huang, Y. Surface ligand engineering of $CsPbBr_3$ perovskite nanowires for high-performance photodetectors. *J. Colloid Interface Sci.* **2022**, *608*, 2367-2376.

[16] Ren, W.; Tan, Q.; Wang, Q.; Liu, Y. Hybrid organolead halide perovskite microwire arrays/single CdSe nanobelt for a high-performance photodetector. *Chem. Eng. J.* **2021**, *406*, 126779.

[17] Li, S. X.; Xu, Y. S.; Li, C. L.; Guo, Q.; Wang, G.; Xia, H.; Fang, H. H.; Shen, L.; Sun, H. B. Perovskite single ‐ crystal microwire ‐ array photodetectors with performance stability

beyond 1 year. *Adv. Mater.* **2020**, *32*, 2001998.

[18] Gao, L.; Zeng, K.; Guo, J.; Ge, C.; Du, J.; Zhao, Y.; Chen, C.; Deng, H.; He, Y.; Song, H. Passivated single-crystalline $CH_3NH_3PbI_3$ nanowire photodetector with high detectivity and polarization sensitivity. *Nano Lett.* **2016**, *16*, 7446-7454.

[19] Waleed, A.; Tavakoli, M. M.; Gu, L.; Wang, Z.; Zhang, D.; Manikandan, A.; Zhang, Q.; Zhang, R.; Chueh, Y.-L.; Fan, Z. Lead-free perovskite nanowire array photodetectors with drastically improved stability in nanoengineering templates. *Nano Lett.* **2017**, *17*, 523-530.

[20] Wu, C. Y.; Peng, W.; Fang, T.; Wang, B.; Xie, C.; Wang, L.; Yang, W. H.; Luo, L. B. Asymmetric contact‐induced self‐driven perovskite‐microwire‐array photodetectors. *Adv. Electron. Mater.* **2019**, *5*, 1900135.

[21] Cao, F.; Tian, W.; Wang, M.; Cao, H.; Li, L. Semitransparent, flexible, and self‐powered photodetectors based on ferroelectricity‐assisted perovskite nanowire arrays. *Adv. Funct. Mater.* **2019**, *29*, 1901280.

[22] Zhou, H.; Song, Z.; Grice, C. R.; Chen, C.; Zhang, J.; Zhu, Y.; Liu, R.; Wang, H.; Yan, Y. Self-powered $CsPbBr_3$ nanowire photodetector with a vertical structure. *Nano Energy* **2018**, *53*, 880-886.

[23] Gui, P.; Chen, Z.; Li, B.; Yao, F.; Zheng, X.; Lin, Q.; Fang, G. High-performance photodetectors based on single all-inorganic $CsPbBr_3$ perovskite microwire. *ACS Photonics* **2018**, *5*, 2113-2119.

[24] Li, C.; Ye, X.; Jiang, J.; Guo, Q.; Zheng, X.; Lin, Q.; Ge, C.; Wang, S.; Chen, J.; Gao, Z. High‐Throughput Growth of Armored Perovskite Single Crystal Fibers for Pixelated Arrays. *Small* **2024**, 2401624.

[25] Dong, K.; Zhou, H.; Gao, Z.; Xu, M.; Zhang, L.; Zhou, S.; Cui, H.; Wang, S.; Tao, C.; Ke, W. 2D Perovskite Single‐Crystalline Photodetector with Large Linear Dynamic Range for UV Weak‐Light Imaging. *Adv. Funct. Mater*. **2024**, *34*, 2306941.

[26] Bao, Y.; Wang, H.; An, M.; Tang, H.; Li, J.; Li, J.; Tan, C.; Luo, Y.; Xu, J.; Yang, Y. Defect-modulated synthesis and optoelectronic properties in chemical vapor deposited $CsPbBr_3$ microplates. *Nano Res.* **2024**, *17*, 4610-4615.

[27] Liu, T.; Wang, J.; Liu, Y.; Min, L.; Wang, L.; Yuan, Z.; Sun, H.; Huang, L.; Li, L.; Meng, X. Cyano‐Coordinated Tin Halide Perovskites for Wearable Health Monitoring and Weak Light

Imaging. *Adv. Mater.* **2024**, 2313946.

[28] Xu, Z.; Pan, X.; Lu, H.; Lu, Q.; Liang, Y.; He, Z.; Zhu, Y.; Yu, Y.; Wu, W.; Han, X. Surface Energy‐Assisted Patterning of Vapor Deposited All‐Inorganic Perovskite Arrays for Wearable Optoelectronics. *Adv. Sci.* **2024**, 2402635.